A Fine Scale Partially Coherent Patch Model including Topographical Effects for GNSS-R DDM Simulations

Haokui Xu[1], Jiyue Zhu[1], Leung Tsang[1, *], and Seung Bum Kim[2]

Abstract—In this paper, we propose a fine scale partially coherent patch model (FPCP) for GNSS-R land applications for soil moisture retrieval. The land surface is divided into coherent planar patches on which microwave roughness is superimposed. The scattered waves of the coherent patch are decomposed into the coherent specular reflection and diffuse incoherent scattering. A fine scale of 2 meter patch size is chosen for the coherent patch to be applicable to complex terrain with large varieties of topographical elevations and with small to large topographical slopes. The summation of scattered fields over patches is carried out using physical optics. The phase term of the scattered wave of each patch is kept so that correlation scattering effects among patches are accounted for. Results are illustrated for power ratio for areas near the specular point and areas far away from the specular point. Comparisons are made with the radiative transfer geometric optics model. DDM simulations are performed with good agreement with CYGNSS data.

1. INTRODUCTION

The Global Navigation Satellite System Reflectometry (GNSS-R) is a new approach for the remote sensing of earth surface. Different from the conventional radar sensors, the GNSS-R utilizes the existing GNSS (e.g., GPS, GLONASS) satellites on-orbit as transmitters and only launches receivers. The operating GNSS-R missions include the Techdemosat-1 (TDS-1) [1] launched by ESA in 2014 and the Cyclone Global Navigation Satellite System (CYGNSS) [2] launched in 2016 by NASA. The GNSS-R data are collected in the form of Delay Doppler Maps (DDMs), which have been applied to the retrieval of ocean wind speed [3], sea ice thickness [4], and monitoring the wetland changes [5]. Recently, researches have also shown the potential of soil moisture retrieval by the GNSS-R data [6–8]. Unlike the existing soil moisture products, the short revisit time of CYGNSS enables a nearly real time soil moisture monitoring, which would be important for applications in disasters like landslides. Benefiting from near-specular scattering, the received power is much larger than that of radar backscattering. This provides the possibility of overcoming forests attenuation effects in the remote sensing of soil moisture in the forested areas.

In recent years, to leverage the soil moisture retrieval based on GNSS-R data, there has been significant research in the physical modelling of the scattering from land surface in GNSS-R bistatic configuration. The traditional models are that of coherent model and incoherent model. Based on the positions of the transmitter and receiver, there are the specular point and Fresnel zones [9]. For the case of CYGNSS, the first Fresnel zone is about 500 meters around the specular point. The coherent model assumes that the terrain is flat, and the received electric field is derived readily such as by using image theorem and the method of stationary phase [10]. An alternative explanation is based on the Fresnel zones with alternate phases with convergence achieved as the sizes of the Fresnel zone decrease

with distances. A centimeter scale microwave roughness with rms height h is also added to describe the attenuation of the coherent wave [11]. The attenuation factor is $\exp(-4k^2h^2\cos^2(\theta_i))$ where θ_i is the incident angle, and k is the wavenumber which is equal to $33\,\mathrm{m}^{-1}$ at the CYGNSS frequency. In the work by Chew and Small [7], the coherent model was used to characterize the land surface scattering for the retrieval of soil moisture. The coherent model is applicable to water body and possibly to wetlands, but the power ratio of received power to transmitted power tends to be many decibels larger than the CYGNSS land data.

The incoherent model is based on the assumption that because of the topological large elevation changes in land surfaces, the received signal is incoherent. Using the concept of incoherent addition in classical radiative transfer theory [12], the intensity of scattered field of land surfaces is obtained by summing the intensities of the intensities from patches (or facets). In addition, the geometric optics approximation [13] is used which assumes that the wavelength, which is 0.19 m at the CYGNSS frequency, is much smaller than the topographical vertical and horizontal distance scales. The scattered intensity is proportional to the probability density function of slopes [13]. The physical interpretation is that the orientation of the patch specularly reflects the incident direction from the transmitter into the direction of the receiver. Let the probability density function be $p_{pdf}(p,q)$ where p and q are the slopes in the horizontal x and y directions, respectively. The choice of pdf is Gaussian so that $p_{pdf}(p,q) = \exp(-(p^2+q^2)/(2s^2))/(2\pi s^2)$ where s is the rms slope, and a small number is usually used. In the incoherent model $p_{pdf}(0,0) = 1/(2\pi s^2)$ is used which means that the scattered intensities come from patches that are horizontal with zero slopes. This assumes that the incident angle of the transmitter θ_i is equal to the scattered angle of the receiver (θ_s). The total power is the incoherent sum from each patch. The model has been used by [14] for the remote sensing of soil moisture. The incoherent mode does not consider the contribution from patches with topographical slopes. The geometric optics approximation depends on the choice of the pdf of the slopes. Two other geometric optics have been developed in [15–17], which have included the effects of topography slope and observation angle change.

In the work of [15], $p_{pdf}(p,q) = p_{pdf}(-k_{dx}/k_{dz}, -k_{dy}/k_{dz})$, where $\overline{k}_d = \overline{k}_i - \overline{k}_s$, $\overline{k}_i$ and $\overline{k}_s$ are respectively the incident wave vector from the transmitter on the patch and the scattered wave vector from the patch to the receiver. This modification takes into account that the incident angles θ_i and θ_s will be different when the patch is far away, such as 10 km, from the specular point, so that the orientation patch needs to be tilted to specular reflect the incident wave into the receiver direction. In applying the model to ocean surfaces, the pdf is constructed from the ocean spectrum such as the Durden-Vesecky spectrum [12]. Arguments are made such that part of the ocean spectrum is used to calculate the pdf of the slopes distribution. The model takes the surface profile fluctuations with ocean spectral wavenumber less than $11\,\mathrm{m}^{-1}$ into account. In Campbell's mode [16, 17], the argument is made that a residue slope (a surface variation scale in between the microwave and topographical scale) was used for the pdf. The factor $p_{pdf}(-k_{dx}/k_{dz}-p, -k_{dy}/k_{dz}-q)$ is used where p and q are the x and y slopes of the patch, respectively. The parameter $s = 0.75°$ is used in the slopes pdf of Gaussian distributions.

Other models include Laura's model [18] which includes both the coherent and incoherent scattering. Laura's model divided the land surface into 300 meter patches. For each patch, the coherent and incoherent scattering were computed [18]. The coherent component is calculated based on the Kirchhoff approximation. Because the patch is large that is beyond the far field limit, a second order Taylor expansion is made in the phase factor. This is the Fresnel approximation of the phase rather than the Franhoeffer linear expansion of the phase. The incoherent intensity is evaluated with the AIEM model. Both topographical slopes and microwave roughness effects were included. In addition, the attenuation factor $\exp(-4k^2h^2\cos^2(\theta_i))$ is used to attenuate the reflection of the patches.

Recently, we have used the wave approach of physical optics by carrying out integration of the Kirchhoff integral. The approach takes into account the finite wavelength and the wave nature of scattering with amplitude and phase as the fine scale topography is comparable to wavelengths. The scattered field is computed by summation under the Kirchhoff integral. The scattered intensity is obtained by taking absolute value of the summed scattered field. In [10], a brute force numerical Kirchhoff simulator that discretized the land surfaces into 2 cm by 2 cm patches is used. Because a large number of patches is used in a 10 km by 10 km area, parallel computation is used for the integration. Simulation results by numerical Kirchhoff show that the topographical elevation destroys the Fresnel zone pattern as on a planar surface. In [19], the land surface is divided into 30 m by 30 m patches. The

coherent scattered wave and incoherent scattered intensity were computed for each patch. The total scattered power is obtained by coherent summation of the coherent waves and incoherent summation of the incoherent intensities over the patches. The two models ignore the variations within 30 meters that will overestimate the coherent effects. Patches are considered as horizontal without topographical slopes. These 2 factors make the model prediction 20 dB greater than data measurements.

In recognizing the effects of fine scale topography change, we propose the fine-scale partially coherent approach for GNSS-R land reflections. In random media scattering, scattering is coherent in small domain. The scattering becomes partially coherent in a domain of intermediate size and becomes incoherent in a large domain. The dividing lines between small and intermediate and between intermediate and large are dependent on problem. The coherence also depends on observation angles. Backscattering at oblique incidence is more incoherent, and the scattering in the forward direction is more coherent. The angular dividing line is also problem dependent. In proposing the partially coherent approach in this paper, we use the fine-scale patch of size of $L = 2\,\text{m}$. We carried out summation of complex fields over N patches. For $N = 1$, the concept of partial coherence is that the scattered field is coherent. For $2 \leq N \leq N_{large}$, the scattered field is partially coherent. For $N > N_{large}$, the scattered field is incoherent. The dividing line of N_{large} can be estimated numerically from the phase distributions of the N_{large} patches.

In surface height characterizations, we consider the surface height as composed of a summation of 3 kinds of roughness/topography.

$$z = f_1(x, y) + f_2(x, y) + f_3(x, y)$$

where $f_1(x, y)$ is the microwave roughness with rms height of 5 cm or less. In the CYGNSS project, extensive measurements are taken to measure the rms heights and correlation lengths of the microwave roughness at supersites. The topography $f_3(x, y)$ is the coarse scale topography as given by Digital Elevation Model (DEM). It is termed coarse because the DEM is of horizontal resolution of 30 m. A linear interpolation is used to obtain $f_3(x, y)$ for continuous variables so that $f_3(x, y)$ corresponds to tilted planar patches. $f_2(x, y)$ is labeled as "fine scale topography" that is in-between the coarse topography and the microwave roughness. The fine scale topography $f_2(x, y)$ will have rms heights of 5 cm and above and horizontal correlations of 0.5 to 10 meters. As shown in this paper, the fine scale topography will significantly influence the GNSS-R land reflections. The proposed partially coherent approach accounts for $f_1(x, y)$ and $f_2(x, y)$ as they are fine-scale, and coherent effects need to be included. In this paper, $f_2(x, y)$ is characterized by uncertainties. Recently, Lidar measurements have been taken [21], and ICESAT2 measurements are also available. For future works, such fine-scale measurements will be used to infer $f_2(x, y)$.

Because the fine topography is not much larger than the CYGNSS wavelength, in this paper, we propose a partially coherent fine scale patch model consisting of discretizing the land surface into small patches such as 2 m by 2 m. The 2 m by 2 m patch can take into account the fine-scale topography. The model is labeled as "Fine-scale partially coherent patch model". We treat the 2 m by 2 m patch as a coherent planar patch on which microwave roughness is superimposed. Salient features of the models are: (i) By using rough surface scattering theory, the scattered wave of the coherent patch is decomposed into the coherent specular reflection and diffuse incoherent scattering. (ii) The diffuse incoherent scattering is derived from the microwave roughness $f_1(x, y)$. (iii) Physical optics are used for the Kirchhoff integral as the fine scale topography is not much larger than the wavelengths. (iv) Since the patch is not large, the phase of the scattered wave by the patch is retained making the model a partially coherent model. (v) It is shown in the limit of increasing the patch size from 2 meters such as to 10 meters, and ignoring the phase term, the partially coherent model reduces to that of the geometric optics model and (vi) Coherent and incoherent waves of the microwave roughness can be calculated by using NMM3D (Numerical Maxwell model of 3 dimensional simulations).

The proposed model is a fine scale partially coherent patch model (FPCP). The total power is obtained by the sum of the absolute square of SWC and SWICI. The SWC is the coherent summation of the weighted coherent fields of the patches, and the SWICI is incoherent summation of the weighted incoherent diffuse intensities. It is important to note that although the coherent field of each patch is coherent, the summation, SWC, can be partially coherent or incoherent because of the random phases among the coherent fields from the patches. Thus the SWC concept is consistent with the classification of coherence of DDM.

Results are illustrated for power ratio for areas near the specular point and areas far away from the specular point. By taking a large patch, the results reduce to that of the RT-GO (radiative transfer geometric optics model). Comparisons are made between the fine scale partial coherent patch model and the RT-GO model.

The paper is organized as follows. In Section 2, the coherent and incoherent scattered waves are derived from a tilted patch using the physical optics approximation of the Kirchhoff integral. Section 3 illustrates the formulation of SWC and SWICI. In Section 4, we show the implementation of SWC and SWICI with the solution of Numerical Maxwell Model 3D (NMM3D) for the microwave roughness. In Section 5, we show the radiative transfer approach. In Section 6, the numerical results are presented. Recently, the topic of interest is the simulation of DDMs that covers an area of 50 km radius. Based on the DDM data, a classification algorithm [20] has been proposed to determine whether the DDM is coherent or incoherent. In this section, we simulate DDMs with the partially coherent model which are compared with CYGNSS data. Then in Section 6 comes with conclusions. In Appendix A, the incoherent diffused intensity of a tilted patch based on NMM3D is given. In Appendix B, we take a special case of the partial coherent model by taking large patches and ignoring the phase term to derive the RT-GO model.

2. KIRCHHOFF MODEL FOR A SINGLE TILTED COHERENT PLANAR PATCH WITH ROUGHNESS

The geometrical configuration of GNSS-R is as shown in Figure 1. In the patch model of terrain, we consider a land surface with multiple elevations and slopes as shown in Figure 2. The specular point is taken to be at the origin $(0, 0, 0)$. As in [19], we divide the land surface into N patches, labeled as $n = 1, 2, 3 \ldots N$ with each patch having a single slope. Because of topography, each patch is tilted from the horizontal plane. Microwave roughness is superimposed on the patch (Figure 2).
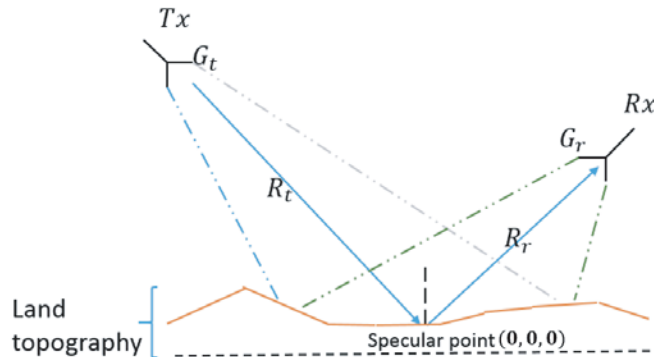
Figure 1. GNSS-R geometry. Specular point at $(0, 0, 0)$.

We calculate the scattering of the patch that consists of the coherent fields and incoherent diffuse intensity. The assumption is that the patch is "coherent" meaning that a decomposition into coherent fields and diffuse incoherent fields in rough surface scattering is applicable. The coherent field is complex and has a definite phase. The diffuse incoherent field has random phase uniformly distributed between 0 and 2π. Thus we compute only the intensity of the diffuse incoherent field. Such a patch will be labeled as a "coherent patch". Let the horizontal projection of each patch be a square of $L \times L$. The coherent patch size chosen in this paper is $L = 2 \, \text{m}$. Let the center of the patch be at (x_n, y_n, z_n), the orientation angle be (β_n, α_n), and the microwave roughness be of h_n rms height and correlation length l_n. By microwave roughness we mean the parameters that center into the calculations of rough surface scattering of the coherent patch. The location (x_n, y_n, z_n) and orientation angle (β_n, α_n) are derived from DEM information. The tilted patch rough surface scattering model is an extension of the horizontal patch model in [12] and [13]. In the following, we suppress, unless necessary, the "n" subscript as the equations are understood to be developed for a single coherent patch.
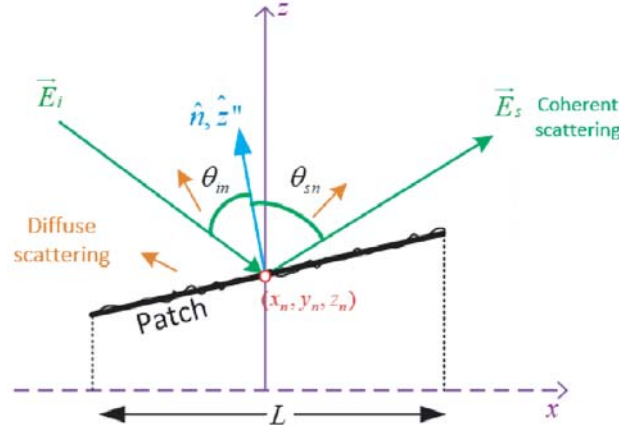
Figure 2. Coherent reelection and diffuse scattering of tilted planar coherent patch with microwave roughness $z'' = f_1(x'', y'')$. Patch center (x_n, y_n, z_n). Fine-scale patch size $L \times L$. Normal to patch $\widehat{n} = \widehat{z}''$; Angles θ_{in} and θ_{sn} are the directions to transmitter and receiver respectively.

2.1. Coordinates and Axes of Tilted Plane

Let the normal vector to the patch be:

$$\widehat{n} = \sin\beta\cos\alpha\widehat{x} + \sin\beta\sin\alpha\widehat{y} + \cos\beta\widehat{z}$$

where $0 \le \alpha \le \frac{\pi}{2}$; $0 \le \beta \le 2\pi$. The normal is also expressed by p and q, the slopes in x and y directions respectively

$$\widehat{n} = \frac{1}{\sqrt{1 + p^2 + q^2}}(-p\widehat{x} - q\widehat{y} + \widehat{z}).$$

The slopes p and q are in terms of α and β:

$$p = -\tan\beta\cos\alpha \tag{1}$$
$$q = -\tan\beta\sin\alpha \tag{2}$$

The microwave roughness is perpendicular to the patch. We use $(\widehat{x}'', \widehat{y}'', \widehat{z}'')$ as the tilted axes where $\widehat{z}''$ coincides with the normal $\widehat{z}'' = \widehat{n}$. Since the two axes, $\widehat{x}''$ and $\widehat{y}''$, are perpendicular to $\widehat{z}''$, and the roughness is assumed to be azimuthal symmetric, we use Eulerian angles of rotations and choose $\gamma = -\alpha$ following the Euler angle notations of [12].

The local coordinates are (x', y', z')

$$x' = x - x_n \tag{3}$$
$$y' = y - y_n \tag{4}$$
$$z' = z - z_n \tag{5}$$

The 3D transformations of coordinates and unit vectors are summarized below. In the following, $(\widehat{x}, \widehat{y}, \widehat{z})$ are labeled as "global" axes and $(\widehat{x}'', \widehat{y}'', \widehat{z}'')$ labeled as "local axes". In the local global axes, the unit vectors are:

$$\widehat{x}' = \widehat{x} \tag{6}$$
$$\widehat{y}' = \widehat{y} \tag{7}$$
$$\widehat{z}' = \widehat{z} \tag{8}$$

The local coordinates are:

$$x'' = (\cos\beta\cos^2\alpha + \sin^2\alpha)x' - \sin\alpha\cos\alpha(1 - \cos\beta)y' + (-\cos\alpha\sin\beta)z' \tag{9}$$
$$y'' = (-\sin\alpha\cos\alpha(1 - \cos\beta))x' + (\cos\beta\sin^2\alpha + \cos^2\alpha)y' + (-\sin\alpha\sin\beta)z' \tag{10}$$
$$z'' = (\sin\beta\cos\alpha)x' + (\sin\beta\sin\alpha)y' + \cos\beta z' \tag{11}$$

and the local unit vectors are:

$$\widehat{x}'' = (\cos\beta\cos^2\alpha + \sin^2\alpha)\widehat{x} - \sin\alpha\cos\alpha(1 - \cos\beta)\widehat{y} + (-\cos\alpha\sin\beta)\widehat{z} \tag{12}$$

$$\widehat{y}'' = (-\sin\alpha\cos\alpha(1 - \cos\beta))\widehat{x} + (\cos\beta\sin^2\alpha + \cos^2\alpha)\widehat{y} + (-\sin\alpha\sin\beta)\widehat{z} \tag{13}$$

$$\widehat{z}'' = \sin\beta\cos\alpha\widehat{x} + \sin\beta\sin\alpha\widehat{y} + \cos\beta\widehat{z} \tag{14}$$

With this choice of γ, the above transformations reduce to familiar forms for small slope which corresponds to small β.

On the surface of the planar patch, there are 2 degrees of freedom as the coordinate $z'' = 0$.

The 2D transformations of the coordinates are then:

$$x' = (\cos\beta\cos^2\alpha + \sin^2\alpha)x'' - \sin\alpha\cos\alpha(1 - \cos\beta)y'' \tag{15}$$

$$y' = -\sin\alpha\cos\alpha(1 - \cos\beta)x'' + (\cos\beta\sin^2\alpha + \cos^2\alpha)y'' \tag{16}$$

We define transformation coefficients:

$$a_{xx} = \sec\beta\cos^2\alpha + \sin^2\alpha \tag{17}$$

$$a_{xy} = a_{yx} = \cos\alpha\sin\alpha(\sec\beta - 1) \tag{18}$$

$$a_{yy} = \sec\beta\sin^2\alpha + \cos^2\alpha \tag{19}$$

Then the inverse transformation is

$$x'' = a_{xx}x' + a_{xy}y' \tag{20}$$

$$y'' = a_{yx}x' + a_{yy}y' \tag{21}$$

In this transformation, the Jacobian is not unity as $dx''dy'' = \sec\beta dx'dy'$. The $\sec\beta$ accounts for the area of the planar patch as $L^2\sec\beta$ that is larger than the horizontal projection of L^2. For small slope β, then $dx''dy'' = dx'dy'$.

2.2. Coherent Scattered Field and Diffuse Incoherent Intensity of the Coherent Patch

Let the GNSS-R transmitter be located at:

$$T_x = (x_t, 0, h_t)$$

and the receiver be located at

$$R_x = (x_r, 0, hr).$$

The distance

$$d = x_r - x_t$$

is the horizontal separation between transmitter and receiver. The specular point is located at $(0, 0, 0)$. Thus:

$$x_r + x_s = d \tag{22}$$

$$x_s = -x_t = \frac{dh_t}{hr + ht} \tag{23}$$

$$x_r = \frac{dh_r}{h_r + h_t} \tag{24}$$

The distances between the patch center and the transmitter and receiver are respectively R_{nt} and R_{nr}:

$$R_{nt} = \sqrt{(x_n - x_t)^2 + y_n^2 + (z_n - h_t)^2} \tag{25}$$

$$R_{nr} = \sqrt{(x_n - x_t)^2 + y_n^2 + (z_n - h_r)^2} \tag{26}$$

In the partially coherent patch model, we keep track of the patch phase term: $\exp(ik(R_{nt} + R_{nr}))$.

The patch size L of $2\,\mathrm{m}$ is small and thus in the far field of both the transmitter and the receiver. This means that both the incident waves and scattered waves are plane waves at the patch. Aside from

the phase term, the distances in the amplitudes of the Green's function are obtained by replacing R_{nt} and R_{nr} respectively by:

$$R_t = \sqrt{(x_t^2 + h_t^2)} \tag{27}$$

$$R_r = \sqrt{(x_r^2 + h_r^2)} \tag{28}$$

The electric field of the incident plane wave on the patch is $\overline{E}_i(\overline{r}'') = \widehat{e}_{in} E_0 \exp(ikR_{nt}) \exp(i\overline{k}_{in} \cdot \overline{r}'')$ where $E_0 = \sqrt{2\eta \frac{P_t G_t}{4\pi R_t^2}}$; η is the wave impedance; P_t and G_t are respectively the power transmitted and the gain of the transmitting antenna. $\widehat{e}_{in}$ is the unit polarization vector which will be chosen to be RHCP. Note that we use $\overline{r}''$ system of the phase term in the incident plane wave. The wave vector of the incident plane wave is:

$$\widehat{k}_{in} = k_{inx}\widehat{x} + k_{iny}\widehat{y} - k_{inz}\widehat{z}$$

where

$$k_{inx} = \frac{k(x_n - x_t)}{R_{nt}} \tag{29}$$

$$k_{iny} = \frac{ky_n}{R_{nt}} \tag{30}$$

$$k_{inz} = \frac{k(h_t - z_n)}{R_{nt}} \tag{31}$$

The incident angle θ_{in} on the patch is:

$$\cos(\theta_{in}) = \frac{k_{inz}}{k}.$$

The incident horizontal and vertical polarizations are:

$$\widehat{h}_{in} = \frac{\widehat{z} \times \widehat{k}_{in}}{|\widehat{z} \times \widehat{k}_{in}|} \tag{32}$$

$$\widehat{v}_{in} = \widehat{h}_{in} \times \widehat{k}_{in} \tag{33}$$

The incident wave is right hand circularly polarized so that

$$\widehat{e}_{in} = \frac{1}{\sqrt{2}}\left(\widehat{v}_{in} + i\widehat{h}_{in}\right).$$

The random rough surface is perpendicular to the planar patch. Thus we use (x'', y'', z'') system to describe the roughness. The microwave centimeter random roughness height function is:

$$z'' = f_1\left(x'', y''\right)$$

where $f_1(x'', y'')$ is a Gaussian random process with rms height h and correlation length l. We shall use exponential correlation functions as it is commonly adopted for land surfaces [22]. The scattered wave is a plane wave with the wave vector

$$\widehat{k}_{sn} = k_{snx}\widehat{x} + k_{sny}\widehat{y} + k_{snz}\widehat{z} \tag{34}$$

$$k_{snx} = \frac{k(x_r - x_n)}{R_{nr}} \tag{35}$$

$$k_{sny} = -\frac{ky_n}{R_{nr}} \tag{36}$$

$$k_{snz} = \frac{k(h_r - z_n)}{R_{nr}} \tag{37}$$

The scattered angle θ_{sn} is $\cos(\theta_{sn}) = \frac{k_{snz}}{k}$. The horizontal and vertical polarization vectors for the scattered wave are:

$$\widehat{h}_{sn} = \frac{\widehat{z} \times \widehat{k}_{sn}}{|\widehat{z} \times \widehat{k}_{sn}|} = \frac{-k_{sny}\widehat{x} + k_{snx}\widehat{y}}{\sqrt{k_{snx}^2 + k_{sny}^2}} \tag{38}$$

$$\widehat{v}_{sn} = \widehat{h}_{sn} \times \widehat{k}_{sn} \tag{39}$$

In the vicinity of the specular point, θ_{sn} is almost identical to θ_{in}. As the location of the patch moves away from the first Fresnel zone, there are small changes in $\widehat{k}_{sn}$ direction because the height of the receiver is much lower than that of the transmitter. The small changes in $\widehat{k}_{sn}$ can cause significant changes in the phase term. The influence on the coherent specular reflection is significant. In using Kirchhoff integral of Equation (2.1.42a) of page 72 of [13], we shall use the scattered field formulation of:

$$\overline{E}_s = \int_{patch} dS'' \left[i\omega\mu\overline{\overline{G}}\left(r, r''\right) \cdot \widehat{n}'' \times \overline{H}_s\left(\overline{r}''\right) + \nabla \times \overline{\overline{G}}\left(r, r''\right) \cdot \widehat{n}'' \times \overline{E}_s\left(\overline{r}''\right) \right] \tag{40}$$

where $\widehat{n}''$ and $\widehat{n}'' \times \overline{E}_s(r'')$ are respectively the tangential scattered magnetic field and the tangential scattered electric field respectively. In [13] the total field formulation was used. The surface integral of the incident fields $\widehat{n} \times \overline{H}_i(r'')$ and $\widehat{n}'' \times \overline{r''}$ of an infinite rough surface is zero:

$$\int\int dS'' \left[i\omega\mu\overline{\overline{G}}\left(r, r''\right) \cdot \widehat{n}'' \times \overline{H}_i\left(r''\right) + \nabla \times \overline{\overline{G}}\left(r, r''\right) \cdot \widehat{n}'' \times \overline{E}_i\left(r''\right) \right] = 0 \tag{41}$$

Thus for an infinite rough surface and if the solutions of Maxwell equations are exact, then the total field formulation and the scattered field formulation are equivalent. However, for the case of finite rough surface and non-exact solutions as inherent in Kirchhoff approximations, the results will be different. The normal $\widehat{n}''$ vector, taking into account of the microwave roughness, is perpendicular to the tangent plane of the rough surface:

$$\widehat{n}'' = \frac{-\dfrac{df_1}{dx''}\widehat{x}'' - \dfrac{df_1}{dy''}\widehat{y}'' + \widehat{z}''}{\sqrt{1 + \left(\dfrac{df_1}{dx''}\right)^2 + \left(\dfrac{df_1}{dy''}\right)^2}}.$$

Then making the tangent plane approximation in Kirchhoff approximation, and carrying out the vector diffraction integral of Equation (30) with a similar derivation to pages 74–76 of [13], but in the (x'', y'', z'') coordinate system:

$$\begin{aligned}
\overline{E}_{sn} &= ik\frac{1}{4\pi R_r}E_0 \exp\left(ik\left(R_{rn} + R_{nt}\right)\right)\left(\widehat{v}_{sn}\widehat{v}_{sn} + \widehat{h}_{sn}\widehat{h}_{sn}\right) \\
&\quad \cdot \int_{patch} dx''dy'' \exp\left(i\left(\overline{k}_{in} - \overline{k}_{sn}\right) \cdot \overline{r}''\right) \overline{F}\left(\frac{df\left(x'', y''\right)}{dx''}, \frac{df\left(x'', y''\right)}{dy''}, \alpha, \beta\right)
\end{aligned}$$

where $\overline{F}(\frac{df(x'')}{dx''}, \frac{df(x'',y'')}{dy''}, \alpha, \beta)$ is in Eq. (2.1.55a) of [13] but with the unity term deleted because of the scattered field formulation instead of total field formulation. The (α, β) in Eq. (2.1.55a) is replaced by $\frac{df_1(x'')}{dx''}$ and $\frac{df_1(x'',y'')}{dy''}$, respectively. Then to carry out the integration analytically, we make approximation of $\overline{F}$ as on pages 81–82 of [13], by setting $\frac{df(x'')}{dx''}$ and $\frac{df(x'',y'')}{dy''}$ to be zero.

$$\overline{F}\left(\frac{df\left(x''\right)}{dx''}, \frac{df\left(x'', y''\right)}{dy''}, \alpha, \beta\right) = \overline{F}\left(0, 0, \alpha, \beta\right)$$

Then as in [13]

$$\overline{F}\left(0, 0, \alpha, \beta\right) = \left[\widehat{q}_{in}R_h\left(\theta_{in}\right)\right]\left(\widehat{e}_{in} \cdot \widehat{q}_{in}\right)\left(\widehat{n} \cdot \widehat{k}_{in}\right) + R_v\left(\theta_{in}\right)\widehat{n} \times \widehat{q}_{in}\left(\widehat{e}_{in} \cdot \widehat{p}_{in}\right)\right] \tag{42}$$

$$+ \left[\widehat{k}_{sn} \times \left(\widehat{n} \times \widehat{q}_{in}\right)\left(\widehat{e}_{in} \cdot \widehat{q}_{in}\right)R_h\left(\theta_{in}\right) - R_v\left(\theta_{in}\right)\widehat{k}_{sn} \times \widehat{q}_{in}\left(\widehat{n} \cdot \widehat{k}_{in}\right)\left(\widehat{e}_{in} \cdot \widehat{p}_{in}\right)\right] \tag{43}$$

in the above equation, the local incidence angle is θ_{li} where

$$\cos(\theta_{in}) = -\widehat{n} \cdot \widehat{k}_{in}$$

also

$$\widehat{q}_{in} = \frac{\widehat{k}_{in} \times \widehat{z}''}{\left|\widehat{k}_{in} \times \widehat{z}''\right|}$$

and

$$\widehat{p}_{in} = \widehat{q}_{in} \times \widehat{k}_{in}$$

The Fresnel reflection coefficients are given by:

$$R_h(\theta_{in}) = \frac{k\cos\theta_{in} - \sqrt{k_1^2 - k^2\sin^2\theta_{in}}}{k\cos\theta_{in} + \sqrt{k_1^2 - k^2\sin^2\theta_{in}}} \tag{44}$$

$$R_v(\theta_{in}) = \frac{\epsilon_1 k\cos\theta_{in} - \epsilon\sqrt{k_1^2 - k^2\sin^2\theta_{in}}}{\epsilon_1 k\cos\theta_{in} + \epsilon\sqrt{k_1^2 - k^2\sin^2\theta_{in}}} \tag{45}$$

where ϵ_1 and k_1 are the permittivity and wavenumber respectively below the rough surface. Then the scattered field of the patch is

$$\overline{E}_{sn} = \frac{ik}{4\pi R_r}E_0\left[\widehat{v}_{sn}\left(\widehat{v}_{sn}\cdot\overline{F}(0,0,\alpha,\beta)\right) + \widehat{h}_{sn}\left(\widehat{h}_{sn}\cdot\overline{F}(0,0,\alpha,\beta)\right)\right]\exp\left(ik\left(R_{nr} + R_{nt}\right)\right)I_p$$

where I_p is the integral:

$$I_p = \int_{patch} dx''dy''\exp\left(i\overline{k}_{dn}\cdot\overline{r}''\right) \tag{46}$$

$$\overline{k}_{dn} = \overline{k}_{in} - \overline{k}_{sn} \tag{47}$$

These analytical approximations are made in addition to the tangent plane approximation unlike the numerical Kirchhoff approach [10]. Basically the microwave roughness is only retained in the phase term with the rest of the integrand ignoring the microwave roughness.

On the rough surface

$$r'' = x''\widehat{x''} + y''\widehat{y''} + f\left(x'',y''\right)\widehat{z}''.$$

Since $\overline{k}_{dn}$ is in $(\widehat{x},\widehat{y},\widehat{z})$ while r'' is in $(\widehat{x}'',\widehat{y}'',\widehat{z}'')$, we let:

$$u = \overline{k}_{dn}\cdot\widehat{x}'' \tag{48}$$

$$v = \overline{k}_{dn}\cdot\widehat{y}'' \tag{49}$$

$$w = \overline{k}_{dn}\cdot\widehat{z}'' \tag{50}$$

Then

$$I_p = \int_{patch} dx''dy''\exp\left(iux'' + iv''\right)\exp\left(iwf\left(x'',y''\right)\right) \tag{51}$$

we decompose I_p into coherent and diffuse incoherent:

$$I_p = \langle I_p\rangle + \left(I_p - \langle I_p\rangle\right)$$

2.3. Coherent Wave $\langle I_p\rangle$

Taking the average, we obtain:

$$\langle I_p\rangle = \exp\left(-\frac{w^2h^2}{2}\right)\int_{patch} dx''dy''\exp\left(iux'' + ivy''\right) \tag{52}$$

To perform the integral, we transform to (x',y') and using the Jacobian. Then we have:

$$\langle I_p\rangle = L^2\exp\left(-\frac{w^2h^2}{2}\right)\sec\beta\,\mathrm{sinc}\left((ua_{xx} + va_{yx})\frac{L}{2}\right)\mathrm{sinc}\left((ua_{xy} + va_{yy})\frac{L}{2}\right) \tag{53}$$

Note that the coherent field intensity is proportional to $|\langle I_p\rangle|^2$ which is proportional to L^4. The coherent scattered field is:

$$\langle\overline{E}_{sn}\rangle = \frac{ik}{4\pi R_r}E_0\exp\left(ikR_{nr} + ikR_{nt}\right)\left(\widehat{v}_{sn}\left(\widehat{v}_{sn}\cdot\overline{F}(0,0,\alpha,\beta)\right) + \widehat{h}_{sn}\left(\widehat{h}_{sn}\cdot\overline{F}(0,0,\alpha,\beta)\right)\right)\langle I_p\rangle \tag{54}$$

The distinct feature of the coherent field of the patch is that it contains the phase term $\exp(ikR_{nr} + ikR_{nt})$. The partially coherent patch model keeps the track of this phase term.

2.4. Diffuse Incoherent $\langle |I_p - \langle I_p \rangle|^2 \rangle$

The diffuse incoherent intensity is [13]

$$\left\langle \left| \overline{E}_{sn} - \langle \overline{E}_{sn} \rangle \right|^2 \right\rangle = \frac{k^2}{16\pi^2 R_r^2} E_0^2 \left(\left| \widehat{v}_{sn} \cdot \overline{F}(0,0,\alpha,\beta) \right|^2 + \left| \widehat{h}_{sn} \cdot \overline{F}(0,0,\alpha,\beta) \right|^2 \right) \left[\left\langle |I_p - \langle I_p \rangle|^2 \right\rangle \right] \quad (55)$$

The integral can be computed in a manner similar to pages 80–81 of [13]. Let the correlation function $C(\rho)$ be defined by:

$$\left\langle f\left(x_1'', y_1''\right) f\left(x_2'', y_2''\right) \right\rangle = h^2 C\left(\sqrt{(x_1'' - x_2'')^2 + (y_1'' - y_2'')^2} \right) \quad (56)$$

For the case of exponential correlation function:

$$C(\rho) = e^{-\frac{\rho}{l}} \quad (57)$$

Then

$$\left\langle |I_p - \langle I_p \rangle|^2 \right\rangle = 2\pi L^2 sec\beta I \quad (58)$$

where

$$I = l^2 \int_0^\infty dx \left[\exp\left(-w^2 h^2 \left(1 - e^{-x}\right)\right) - \exp\left(-w^2 h^2\right) \right] J_0\left(\sqrt{u^2 + v^2} lx\right) \quad (59)$$

and J_0 is the Bessel function of order 0. The integral I can be calculated numerically for any h and l. For the case of small to moderate h, it is convenient to make Taylor expansions. Then we have:

$$\left\langle |I_p - \langle I_p \rangle|^2 \right\rangle = 2\pi L^2 l^2 \sec\beta \exp\left(-w^2 h^2\right) \sum_{m=1}^{\infty} \frac{(wh)^{2m}}{m!} \frac{m}{\left(m^2 + l^2\left(u^2 + v^2\right)\right)^{\frac{3}{2}}} \quad (60)$$

where exponential correlation function is assumed. Note that $\langle |I_p - \langle I_p \rangle|^2 \rangle$ is proportional to $L^2 l^2$ showing that the magnitude of diffuse incoherent intensity depends significantly on the measured correlation length l.

3. SWC AND SWICI

3.1. SWC: Summation for Coherent Fields

We sum the coherent field of N patches. The summation of coherent fields is labeled as SWC: summation of weighted coherent field. The weighting is due to the property of the orientation angles of the patch and the microwave rms height of each patch.

$$\overline{E}_s^{SWC} = \sum_{n=1}^{N} \langle \overline{E}_{sn} \rangle$$

$$= \sum_{n=1}^{N} \frac{ik}{4\pi R_r} E_0 \left[\widehat{v}_{sn} \left(\widehat{v}_{sn} \cdot \overline{F}(0,0,\alpha_n,\beta_n) \right) + \widehat{h}_{sn} \widehat{h}_{sn} \cdot \overline{F}(0,0,\alpha_n,\beta_n) \right] \exp\left(ikR_{nr} + ikR_{nt}\right) \langle I_{pn} \rangle$$

where:

$$\langle I_p \rangle = L^2 \exp\left(-\frac{w^2 h^2}{2}\right) \sec\beta_n \mathrm{sinc}\left((ua_{xx} + va_{yx})_n \frac{L}{2}\right) \mathrm{sinc}\left((ua_{xy} + va_{yy})_n \frac{L}{2}\right) \quad (61)$$

The received power P_r is

$$P_r = \frac{|E_s|^2}{2\eta} \frac{G_r \lambda^2}{4\pi} \quad (62)$$

where G_r is the gain of the receiving antenna, and λ is the wavelength. Substituting in the expression for E_0, the power ratio for SWC:

$$\frac{P_r^{SWC}}{P_t} = \frac{G_r G_t}{64\pi^2 R_r^2 R_t^2} \left| \sum_{n=1}^{N} \exp\left(ik\left(R_{nr} + R_{nt}\right)\right) \left(\widehat{v}_{sn}\left(\widehat{v}_{sn} \cdot \overline{F}\left(0,0,\alpha_n,\beta_n\right)\right)\right.\right.$$

$$\left.\left. +\widehat{h}_{sn}\left(\widehat{h}_{sn} \cdot \overline{F}\left(0,0,\alpha_n,\beta_n\right)\right)\right) \langle I_{pn} \rangle \right|^2 \tag{63}$$

The power in SWC is a partially coherent model result.

(1) In the summation over n, there is a patch phase term $\exp(ik(R_{nr} + R_{nt}))$ that accounts for the phase dependence. The coherent fields of the patches are summed.

(2) The coherent field from each coherent patch is coherent, but the summation of coherent fields of N patches can make the summed SWC field partially coherent or incoherent.

(3) In using $L = 2$ meter patches, the summation over a moderate number of patches is partially coherent but can become incoherent as the number of patches further increases.

(4) In preserving the phase, the SWC model is also applicable to water body and wetlands.

(5) Note that $\langle I_{pn} \rangle$ has L^2 factor so that the RHS of the equation for $\frac{P_r^{SWC}}{P_t}$ is dimensionless.

3.2. SWICI: Summation of Diffuse Incoherent Intensity

For the incoherent diffuse intensity, we sum the intensity of each patch to obtain the SWICI.

$$\frac{Pr^{SWCICI}}{Pt} = \frac{G_r G_t}{64\pi^2 R_r^2 R_t^2} \sum_{n=1}^{N} \left(\left|\widehat{v}_{sn} \cdot \overline{F}\left(0,0,\alpha_n,\beta_n\right)\right|^2 + \left|\widehat{h}_{sn} \cdot \overline{F}\left(0,0,\alpha_n,\beta_n\right)\right|^2 \right) \left\langle \left|I_p - \langle I_p \rangle\right|^2 \right\rangle_n \tag{64}$$

3.3. Small Slope Approximation, $\beta \ll 1$, of SWC and SWICI

The SWC and SWICI formulas are applicable to general topographical slopes. The formulas simplify considerably by making the small slope assumption on the topographical slopes. Most of the terrains have Small slopes. Let $\beta \ll 1$, then

$$\sin\beta = \beta; \quad \cos\beta = 1, \sec\beta = 1 \quad a_{xx} = 1; \quad a_{yx} = a_{xy} = 0; \quad a_{yy} = 1$$

We also make the approximation that k_{dnx} and k_{dy} are small because the incident angle is close to the scattered angle. The terms k_{dnx} and k_{dy} can be set to zero except for those terms that are multiplied by a large number such as the patch size, or they are divided by a small number such as topographical slope. Then for small slopes,

$$u = k_{dnx} + k_{dnz}p$$
$$v = k_{dny} + k_{dnz}q$$
$$w = k_{dnz} = -2k\cos\theta_i$$
$$\frac{w_n^2 h_n^2}{2} = 2k^2 h^2 \cos^2\theta_i$$

The Fresnel coefficient dependent $\overline{F}(0,0,\alpha_n,\beta_n)$ can be approximated by

$$\left(\widehat{v}_{sn}\left(\widehat{v}_{sn} \cdot \overline{F}\left(0,0,\alpha_n,\beta_n\right)\right) + \widehat{h}_{sn} \cdot \overline{F}\left(0,0,\alpha_n,\beta_n\right)\widehat{h}_{sn}\right)$$

$$= \left(-2\cos\theta_i\right) \frac{\left[\widehat{v}_s\left(R_v\left(\theta_i\right)\right) + i\widehat{h}_s R_h\left(\theta_i\right)\right]}{\sqrt{2}}$$

where right hand circularized polarized incident wave is assumed. Then the SWC power ratio is simplified to

$$\frac{P_r^{SWC}}{P_t} = \frac{G_r G_t}{64\pi^2 R_r^2 R_t^2} \left| \sum_{n=1}^{N} L^2 e^{ik(R_{nr}+R_{nt})} e^{-2k^2 h_n^2 \cos^2 \theta_i} \text{sinc}\left(\left(\frac{k_{dnx}}{k_{dnz}} + p_n \right) \frac{k_{dnz}L}{2} \right) \right.$$

$$\left. \text{sinc}\left(\left(\frac{k_{dny}}{k_{dnz}} + q_n \right) \frac{k_{dnz}L}{2} \right) \left[\frac{2\cos\theta_i \left[\widehat{v}_s \left(R_v \left(\theta_i \right) \right) + i \widehat{h}_s R_h \left(\theta_i \right) \right]}{\sqrt{2}} \right] \right|^2 \quad (65)$$

As explained in the introduction, in proposing the partially coherent approach in this paper, we use fine-scale patch size of $L = 2\,\text{m}$. We carried out summation of complex fields over N patches. For $N = 1$, the concept of partial coherence is that the scattered field is coherent. For $2 < N < N_{large}$, the scattered field is partially coherent. For $N > N_{large}$, the scattered field is incoherent. The dividing line of N_{large} can be estimated numerically from the $\exp(ik(R_{nr} + R_{nt}))$ factors that give the phase distributions for the N_{large} patches.

The sinc function is equal to the maximum of unity when the argument is equal to zero. Thus the peaks are at $(\frac{k_{dnx}}{k_{dnz}} + p_n)$ and $(\frac{k_{dny}}{k_{dnz}} + q_n)$ both equal to zero. These correspond to the case when the slopes of the patch specularly reflect to the receiver. Near the specular points $\frac{k_{dnx}}{k_{dnz}}$ and $\frac{k_{dny}}{k_{dnz}}$ are equal to zero, so that p_n and q_n need to be zero to specularly reflect to the receiver. Far away from specular point, $\frac{k_{dnx}}{k_{dnz}}$ and $\frac{k_{dny}}{k_{dnz}}$ are not equal to zero, then the orientation of the patch needs to be favorably tilted to reflect to the receiver.

For the fine-scale partially coherent model, the patch size is chosen to be $L = 2\,\text{m}$. The expressions derived apply to all patch sizes. We consider the special case of the RT (radiative transfer). The RT model is by taking the absolute value squared of the term inside the summation and followed by summation. This means that the phase term is discarded:

$$\frac{P_r^{SWC-RT}}{P_t} = \frac{G_r G_t}{64\pi^2 R_r^2 R_t^2} \sum_{n=1}^{N} L^4 e^{-4k^2 h_n^2 \cos^2 \theta_i} 4\cos^2 \theta_i \left| R_{CP} \left(\theta_i \right) \right|^2$$

$$\text{sinc}^2 \left(\left(\frac{k_{dnx}}{k_{dnz}} + p_n \right) \frac{k_{dnz}L}{2} \right) \text{sinc}^2 \left(\left(\frac{k_{dny}}{k_{dnz}} + q_n \right) \frac{k_{dnz}L}{2} \right) \quad (66)$$

In Appendix B, Geometric optics is applied by using large patches such as $L = 10\,\text{m}$, $30\,\text{m}$. Combining the two gives the RT-GO model.

The SWICI power ratio is simplified to

$$\frac{P_r^{SWICI}}{P_t} = \frac{G_r G_t}{64\pi^2 R_r^2 R_t^2} \sum_{n=1}^{N} 4\cos^2 \theta_i \left| R_{CP} \left(\theta_i \right) \right|^2 \left[\left\langle |I_p|^2 \right\rangle - |\langle I_p \rangle|^2 \right] \quad (67)$$

where $|R_{CP}(\theta_i)|^2 = \frac{|R_v(\theta_i)|^2 + |R_h(\theta_i)|^2}{2}$ is the reflectivity of CP (circularly polarized) waves, and $\left\langle |I_p|^2 \right\rangle - |\langle I_p \rangle|^2$ is simplified to

$$\left\langle |I_p|^2 \right\rangle - |\langle I_p \rangle|^2$$

$$= 2\pi L^2 \ell^2 \exp\left(-4k^2 h^2 \cos^2 \theta_i \right) \sum_{m=1}^{\infty} \frac{\left(4k^2 h^2 \cos^2 \theta_i \right)^m}{(m-1)! \left(m^2 + \ell^2 \left((k_{dnx} + k_{dnz}p)^2 + (k_{dny} + k_{dnz}q)^2 \right) \right)^{\frac{3}{2}}}$$

4. NMM3D FOR A TILTED PLANAR PATCH WITH ROUGH SURFACE

The scattering by microwave roughness can be obtained by Numerical solutions of Maxwell equations (NMM3D). We have extensively solved Maxwell equations using Numerical solutions of Maxwell equations NMM3D [22, 23]. These solutions were performed at L band for the SMAP project [24–26]. The rough surface is characterized by exponential correlation functions with rms height h and

correlation length l. Monte Carlo simulations are performed. In Monte Carlo simulation, for each realization of random rough surface, an incident tapered wave is incident on the rough surface with vertical polarization and with horizontal polarization. The scattered fields for each realization are calculated over 2π solid angle of the hemisphere. The computed data for each realization were stored. Using such data, speckle statistics were calculated [27].

Using such computed data, the incoherent bistatic scattering coefficients are calculated by taking averages over realizations followed by subtraction of the coherent field. The computed backscattering coefficients are in good agreement with measurement data [25, 26, 28]. Because a tapered wave is used, the coherent wave has an angular spreading in the specular direction. In the following, we describe how these computed data are used to compute the power ratios of SWC and SWICI for a tilted planar patch with random rough surface. The recorded simulations data are in terms of local incidence angle, local scattered angle, and local h and v polarizations of the tilted patch.

For a planar patch with the normal vector $\widehat{n}$, the local incident angle θ_{li} obeys

$$\cos\theta_{li} = -\widehat{k}_{in} \cdot \widehat{n}$$

The local scattered angle θ_{ls} obeys

$$\cos\theta_{ls} = \widehat{k}_{sn} \cdot \widehat{n}$$

NMM3D table is based on the bistatic scattering coefficient

$$\gamma_{\chi_l \kappa_l}(\theta_{ls}, \phi_{ls} - \phi_{li}; \theta_{li}, 0)$$

where χ_l, κ_l are polarizations defined locally. Because of azimuthal symmetry of roughness, the dependence of $\gamma_{\chi_l \kappa_l}$ is on $\phi_{ls} - \phi_{li}$. From the local incident and scattered direction of the patch $\widehat{k}_{in}$ and $\widehat{k}_{sn}$, we have

$$\sin\theta_{li}\sin\theta_{ls}\cos(\phi_{ls} - \phi_{li}) = \widehat{k}_{in} \cdot \widehat{k}_{sn} + \cos\theta_{li}\cos\theta_{ls}$$

from which ϕ_{ls}, ϕ_{li} can be obtained. For the tilted patch, the local perpendicular polarization is

$$\widehat{h}_{in}^l = \frac{\widehat{n} \times \widehat{k}_{in}}{|\widehat{n} \times \widehat{k}_{in}|}$$

and the local vertical polarization is

$$\widehat{v}_{in}^l = \widehat{h}_{in}^l \times \widehat{k}_{in}$$

The local scattered horizontal polarization vector is:

$$\widehat{h}_{sn}^l = \frac{\widehat{n} \times \widehat{k}_{sn}}{|\widehat{n} \times \widehat{k}_{sn}|}$$

The local scattered vertical polarization vector is:

$$\widehat{v}_{sn}^l = \widehat{h}_{sn}^l \times \widehat{k}_{sn}$$

We express the incident unit amplitude RHCP $\widehat{e}_{in}$ waves in terms of local polarization

$$\overline{E}_i = E_{vi}^i \widehat{v}_{in}^l + E_{hi}^i \widehat{h}_{in}^l$$

where

$$E_{vi} = \widehat{v}_{in}^l \cdot \widehat{e}_{in}$$

and

$$E_{hi} = \widehat{h}_{in}^l \cdot \widehat{e}_{in}$$

The incident polarization can be expressed in terms of 4 stokes parameters:

$$\begin{bmatrix} \left|E_{v_\ell}^i\right|^2 \\ \left|E_{h_\ell}^i\right|^2 \\ E_{v_\ell}^i E_{h_\ell}^{i*} \\ E_{v_\ell}^{i*} E_{h_\ell}^i \end{bmatrix}$$

The scattered wave is

$$\overline{E}_s = E^s_{v_\ell} \widehat{v}^{(\ell)}_{sn} + E^s_{h_\ell} \widehat{h}^{(\ell)}_{sn}$$

The 4 Stokes parameters of the scattered wave are

$$\begin{bmatrix} \left|E^s_{v_\ell}\right|^2 \\ \left|E^s_{h_\ell}\right|^2 \\ E^s_{v_\ell} E^{s*}_{h_\ell} \\ E^{s*}_{v_\ell} E^s_{h_\ell} \end{bmatrix}$$

4.1. NMM3D Diffused Scattering

The diffused components of the scattering of NMM3D can be obtained from the $\overline{\overline{\Gamma}}^{NMM3D,dif}(\theta_{\ell s}, \phi_{\ell s} - \phi_{\ell i}, \theta_{\ell i,} 0)$ matrix

$$\begin{bmatrix} \left|E^s_{v_\ell}\right|^2 \\ \left|E^s_{h_\ell}\right|^2 \\ E^s_{v_\ell} E^{s*}_{h_\ell} \\ E^{s*}_{v_\ell} E^s_{h_\ell} \end{bmatrix}_{dif} = \frac{1}{R_r^2} \frac{A_P \cos\theta_{\ell i}}{4\pi} \overline{\overline{\Gamma}}^{NMM3D,dif}(\theta_{\ell s}, \phi_{\ell s} - \phi_{\ell i}, \theta_{\ell i}, 0) \begin{bmatrix} \left|E^i_{v_\ell}\right|^2 \\ \left|E^i_{h_\ell}\right|^2 \\ E^i_{v_\ell} E^{i*}_{h_\ell} \\ E^{i*}_{v_\ell} E^i_{h_\ell} \end{bmatrix}$$

where $A_P = L^2 \sec\beta$. The $\overline{\overline{\Gamma}}^{NMM3Ddiff}$ matrix is derived in appendix. Then the global vertically polarized component and horizontally polarized component of the scattered waves are:

$$\widehat{v}_{sn} \cdot \overline{E}_s = E^s_{v_\ell} \left(\widehat{v}_{sn} \cdot \widehat{v}^{(\ell)}_{sn}\right) + E^s_{h_\ell} \left(\widehat{v}_{sn} \cdot \widehat{h}^{(\ell)}_{sn}\right)$$

$$\widehat{h}_{sn} \cdot \overline{E}_s = E^s_{v_\ell} \left(\widehat{h}_{sn} \cdot \widehat{v}^{(\ell)}_{sn}\right) + E^s_{h_\ell} \left(\widehat{h}_{sn} \cdot \widehat{h}^{(\ell)}_{sn}\right)$$

The Stokes vector for the diffused scattered wave is:

$$\begin{bmatrix} \left|\widehat{v}_{sn} \cdot \overline{E}_s\right|^2 \\ \left|\widehat{h}_{sn} \cdot \overline{E}_s\right|^2 \\ \left(\widehat{v}_{sn} \cdot \overline{E}_s\right)\left(\widehat{h}_{sn} \cdot \overline{E}_s\right)^* \\ \left(\widehat{v}_{sn} \cdot \overline{E}_s\right)^*\left(\widehat{h}_{sn} \cdot \overline{E}_s\right) \end{bmatrix}$$

$$= \begin{bmatrix} \left(\widehat{v}_{sn} \cdot \widehat{v}^{(\ell)}_{sn}\right)^2 & \left(\widehat{v}_{sn} \cdot \widehat{h}^{(\ell)}_{sn}\right)^2 & \left(\widehat{v}_{sn} \cdot \widehat{v}^{(\ell)}_{sn}\right)\left(\widehat{v}_{sn} \cdot \widehat{h}^{(\ell)}_{sn}\right) & \left(\widehat{v}_{sn} \cdot \widehat{v}^{(\ell)}_{sn}\right)\left(\widehat{v}_{sn} \cdot \widehat{h}^{(\ell)}_{sn}\right) \\ \left(\widehat{h}_{sn} \cdot \widehat{v}^{(\ell)}_{sn}\right)^2 & \left(\widehat{h}_{sn} \cdot \widehat{h}^{(\ell)}_{sn}\right)^2 & \left(\widehat{h}_{sn} \cdot \widehat{v}^{(\ell)}_{sn}\right)\left(\widehat{h}_{sn} \cdot \widehat{h}^{(\ell)}_{sn}\right) & \left(\widehat{h}_{sn} \cdot \widehat{v}^{(\ell)}_{sn}\right)\left(\widehat{h}_{sn} \cdot \widehat{h}^{(\ell)}_{sn}\right) \\ \left(\widehat{v}_{sn} \cdot \widehat{v}^{(\ell)}_{sn}\right)\left(\widehat{h}_{sn} \cdot \widehat{v}^{(\ell)}_{sn}\right) & \left(\widehat{v}_{sn} \cdot \widehat{h}^{(\ell)}_{sn}\right)\left(\widehat{h}_{sn} \cdot \widehat{h}^{(\ell)}_{sn}\right) & \left(\widehat{v}_{sn} \cdot \widehat{v}^{(\ell)}_{sn}\right)\left(\widehat{h}_{sn} \cdot \widehat{h}^{(\ell)}_{sn}\right) & \left(\widehat{v}_{sn} \cdot \widehat{h}^{(\ell)}_{sn}\right)\left(\widehat{h}_{sn} \cdot \widehat{v}^{(\ell)}_{sn}\right) \\ \left(\widehat{v}_{sn} \cdot \widehat{v}^{(\ell)}_{sn}\right)\left(\widehat{h}_{sn} \cdot \widehat{v}^{(\ell)}_{sn}\right) & \left(\widehat{v}_{sn} \cdot \widehat{h}^{(\ell)}_{sn}\right)\left(\widehat{h}_{sn} \cdot \widehat{h}^{(\ell)}_{sn}\right) & \left(\widehat{v}_{sn} \cdot \widehat{h}^{(\ell)}_{sn}\right)\left(\widehat{h}_{sn} \cdot \widehat{v}^{(\ell)}_{sn}\right) & \left(\widehat{v}_{sn} \cdot \widehat{v}^{(\ell)}_{sn}\right)\left(\widehat{h}_{sn} \cdot \widehat{h}^{(\ell)}_{sn}\right) \end{bmatrix}$$

$$\begin{bmatrix} \left|E^s_{v_\ell}\right|^2 \\ \left|E^s_{h_\ell}\right|^2 \\ E^s_{v_\ell} E^{s*}_{h_\ell} \\ E^{s*}_{v_\ell} E^s_{h_\ell} \end{bmatrix}$$

Combining the equations gives

$$
\begin{bmatrix}
\left|\widehat{v}_{sn} \cdot \overline{E}_s\right|^2 \\
\left|\widehat{h}_{sn} \cdot \overline{E}_s\right|^2 \\
\left(\widehat{v}_{sn} \cdot \overline{E}_s\right)\left(\widehat{h}_{sn} \cdot \overline{E}_s\right)^* \\
\left(\widehat{v}_{sn} \cdot \overline{E}_s\right)^*\left(\widehat{h}_{sn} \cdot \overline{E}_s\right)
\end{bmatrix}_{uit\,amplitude\,of\,incident\,RHCP}
$$

$$
= \begin{bmatrix}
\left(\widehat{v}_{sn} \cdot \widehat{v}_{sn}^{(\ell)}\right)^2 & \left(\widehat{v}_{sn} \cdot \widehat{h}_{sn}^{(\ell)}\right)^2 & \left(\widehat{v}_{sn} \cdot \widehat{v}_{sn}^{(\ell)}\right)\left(\widehat{v}_{sn} \cdot \widehat{h}_{sn}^{(\ell)}\right) & \left(\widehat{v}_{sn} \cdot \widehat{v}_{sn}^{(\ell)}\right)\left(\widehat{v}_{sn} \cdot \widehat{h}_{sn}^{(\ell)}\right) \\
\left(\widehat{h}_{sn} \cdot \widehat{v}_{sn}^{(\ell)}\right)^2 & \left(\widehat{h}_{sn} \cdot \widehat{h}_{sn}^{(\ell)}\right)^2 & \left(\widehat{h}_{sn} \cdot \widehat{v}_{sn}^{(\ell)}\right)\left(\widehat{h}_{sn} \cdot \widehat{h}_{sn}^{(\ell)}\right) & \left(\widehat{h}_{sn} \cdot \widehat{v}_{sn}^{(\ell)}\right)\left(\widehat{h}_{sn} \cdot \widehat{h}_{sn}^{(\ell)}\right) \\
\left(\widehat{v}_{sn} \cdot \widehat{v}_{sn}^{(\ell)}\right)\left(\widehat{h}_{sn} \cdot \widehat{v}_{sn}^{(\ell)}\right) & \left(\widehat{v}_{sn} \cdot \widehat{h}_{sn}^{(\ell)}\right)\left(\widehat{h}_{sn} \cdot \widehat{h}_{sn}^{(\ell)}\right) & \left(\widehat{v}_{sn} \cdot \widehat{v}_{sn}^{(\ell)}\right)\left(\widehat{h}_{sn} \cdot \widehat{h}_{sn}^{(\ell)}\right) & \left(\widehat{v}_{sn} \cdot \widehat{h}_{sn}^{(\ell)}\right)\left(\widehat{h}_{sn} \cdot \widehat{v}_{sn}^{(\ell)}\right) \\
\left(\widehat{v}_{sn} \cdot \widehat{v}_{sn}^{(\ell)}\right)\left(\widehat{h}_{sn} \cdot \widehat{v}_{sn}^{(\ell)}\right) & \left(\widehat{v}_{sn} \cdot \widehat{h}_{sn}^{(\ell)}\right)\left(\widehat{h}_{sn} \cdot \widehat{h}_{sn}^{(\ell)}\right) & \left(\widehat{v}_{sn} \cdot \widehat{h}_{sn}^{(\ell)}\right)\left(\widehat{h}_{sn} \cdot \widehat{v}_{sn}^{(\ell)}\right) & \left(\widehat{v}_{sn} \cdot \widehat{v}_{sn}^{(\ell)}\right)\left(\widehat{h}_{sn} \cdot \widehat{h}_{sn}^{(\ell)}\right)
\end{bmatrix}
$$

$$
\frac{1}{R_r^2}\frac{L^2 \sec\beta \cos\theta_{\ell i}}{4\pi}\overline{\overline{\Gamma}}^{NMM3D}(\theta_{\ell s}, \phi_{\ell s} - \phi_{\ell i}, \theta_{\ell i}, 0)
\begin{bmatrix}
\left|E_{v_\ell}^i\right|^2 \\
\left|E_{h_\ell}^i\right|^2 \\
E_{v_\ell}^i E_{h_\ell}^{i*} \\
E_{v_\ell}^{i*} E_{h_\ell}^i
\end{bmatrix}
$$

The bistatic scattering coefficient for the diffuse incoherent wave of the patch is

$$
\gamma_{n,diff} = \frac{1}{4\pi \cos\theta_i}\frac{1}{L^2}\left(4\pi\right)^2 R_r^2 \left[\left|\widehat{v}_{sn} \cdot \overline{E}_s\right|^2 + \left|\widehat{h}_{sn} \cdot \overline{E}_s\right|^2\right]_{uni\,RHCP\,incident\,amplitude}
$$

We define

$$
\overline{Q}^{tilted} = \begin{bmatrix}
Q_1^{tilted} \\
Q_2^{tilted} \\
Q_3^{tilted} \\
Q_4^{tilted}
\end{bmatrix}
$$

$$
= \begin{bmatrix}
\left(\widehat{v}_{sn} \cdot \widehat{v}_{sn}^{(\ell)}\right)^2 & \left(\widehat{v}_{sn} \cdot \widehat{h}_{sn}^{(\ell)}\right)^2 & \left(\widehat{v}_{sn} \cdot \widehat{v}_{sn}^{(\ell)}\right)\left(\widehat{v}_{sn} \cdot \widehat{h}_{sn}^{(\ell)}\right) & \left(\widehat{v}_{sn} \cdot \widehat{v}_{sn}^{(\ell)}\right)\left(\widehat{v}_{sn} \cdot \widehat{h}_{sn}^{(\ell)}\right) \\
\left(\widehat{h}_{sn} \cdot \widehat{v}_{sn}^{(\ell)}\right)^2 & \left(\widehat{h}_{sn} \cdot \widehat{h}_{sn}^{(\ell)}\right)^2 & \left(\widehat{h}_{sn} \cdot \widehat{v}_{sn}^{(\ell)}\right)\left(\widehat{h}_{sn} \cdot \widehat{h}_{sn}^{(\ell)}\right) & \left(\widehat{h}_{sn} \cdot \widehat{v}_{sn}^{(\ell)}\right)\left(\widehat{h}_{sn} \cdot \widehat{h}_{sn}^{(\ell)}\right) \\
\left(\widehat{v}_{sn} \cdot \widehat{v}_{sn}^{(\ell)}\right)\left(\widehat{h}_{sn} \cdot \widehat{v}_{sn}^{(\ell)}\right) & \left(\widehat{v}_{sn} \cdot \widehat{h}_{sn}^{(\ell)}\right)\left(\widehat{h}_{sn} \cdot \widehat{h}_{sn}^{(\ell)}\right) & \left(\widehat{v}_{sn} \cdot \widehat{v}_{sn}^{(\ell)}\right)\left(\widehat{h}_{sn} \cdot \widehat{h}_{sn}^{(\ell)}\right) & \left(\widehat{v}_{sn} \cdot \widehat{h}_{sn}^{(\ell)}\right)\left(\widehat{h}_{sn} \cdot \widehat{v}_{sn}^{(\ell)}\right) \\
\left(\widehat{v}_{sn} \cdot \widehat{v}_{sn}^{(\ell)}\right)\left(\widehat{h}_{sn} \cdot \widehat{v}_{sn}^{(\ell)}\right) & \left(\widehat{v}_{sn} \cdot \widehat{h}_{sn}^{(\ell)}\right)\left(\widehat{h}_{sn} \cdot \widehat{h}_{sn}^{(\ell)}\right) & \left(\widehat{v}_{sn} \cdot \widehat{h}_{sn}^{(\ell)}\right)\left(\widehat{h}_{sn} \cdot \widehat{v}_{sn}^{(\ell)}\right) & \left(\widehat{v}_{sn} \cdot \widehat{v}_{sn}^{(\ell)}\right)\left(\widehat{h}_{sn} \cdot \widehat{h}_{sn}^{(\ell)}\right)
\end{bmatrix}
$$

$$
\sec\beta \cos\theta_{\ell i}
$$

$$
\overline{\overline{\Gamma}}^{NMM3D,dif}(\theta_{\ell s}, \phi_{\ell s} - \phi_{\ell i}, \theta_{\ell i}, 0)
\begin{bmatrix}
\left|E_{v_\ell}^i\right|^2 \\
\left|E_{h_\ell}^i\right|^2 \\
E_{v_\ell}^i E_{h_\ell}^{i*} \\
E_{v_\ell}^{i*} E_{h_\ell}^i
\end{bmatrix}
$$

Thus

$$
\gamma_{n,diff} = \frac{1}{\cos\theta_i}\left[Q_1^{tilted} + Q_2^{tilted}\right]
$$

The power ratio of SWICI for NMM3D is then

$$\frac{P_r^{SWICI}}{P_t} = \frac{G_t G_r \lambda^2}{64\pi^3 R_t^2 R_r^2} \sum_n L^2 \left[Q_1^{tilted} + Q_2^{tilted} \right]$$

4.2. NMM3D Coherent Wave Complex Amplitude for Tilted Patch

As stated earlier, we need to calculate the coherent wave complex amplitude for a tilted patch. For NMM3D, we cannot use peak amplitude of the coherent wave in the specular direction because the tapered wave is used in NMM3D which causes angular spreading of the coherent wave so that the peak amplitude depends on the tapering of the incident wave. We calculate the coherent wave complex amplitude using the following approach.

We first calculate the reflectivity of the coherent wave which contributes to the emissivity of passive remote sensing [23].

a) For vertical incidence we calculate, by integration

$$r_v^{coh}(\theta_i) = \frac{1}{4\pi} \int_0^{\pi/2} d\theta_s \sin\theta_s \int_0^{2\pi} d\phi_s \left[\gamma_{vv}^{coh}(\theta_s, \phi_s, \theta_i, 0) + \gamma_{hv}^{coh}(\theta_s, \phi_s, \theta_i, 0) \right] \tag{68}$$

The integration includes the angular spreading of the coherent wave to get the total power of the coherent wave.

b) For horizontal polarized incidence, we have

$$r_h^{coh}(\theta_i) = \frac{1}{4\pi} \int_0^{\pi/2} d\theta_s \sin\theta_s \int_0^{2\pi} d\phi_s \left[\gamma_{vh}^{coh}(\theta_s, \phi_s, \theta_i, 0) + \gamma_{hh}^{coh}(\theta_s, \phi_s, \theta_i, 0) \right] \tag{69}$$

We next use an analogy to the Kirchhoff approximation for a patch of finite size. There is also angular spreading in the sinc functions of the KA approach. For a large patch size L much larger than the wavelength, the integration of sinc^2 gives

$$\int_0^{\pi/2} d\theta_s \sin\theta_s \int_0^{2\pi} d\phi_s \exp\left(-k_{dz}^2 h^2\right) \text{sinc}^2\left(k_{dx}\frac{L}{2}\right) \text{sinc}^2\left(k_{dy}\frac{L}{2}\right)$$

$$= \frac{4\pi^2}{k^2 L^2 \cos\theta_i} \exp\left(-4h^2 k_{iz}^2\right)$$

Thus for KA:

$$\sqrt{r_v^{coh,KA}} = |R_{v0}| \exp\left(-2h^2 k_{iz}^2\right) \tag{70}$$

$$\sqrt{r_h^{coh,KA}} = |R_{h0}| \exp\left(-2h^2 k_{iz}^2\right) \tag{71}$$

For the phase, we also use an analogy. For vertical polarized incidence,

$$\widehat{v}_s \cdot \overline{F}(0,0) = -2R_{v0}\cos\theta_i \tag{72}$$

$$\widehat{h}_s \cdot \overline{F}(0,0) = 0 \tag{73}$$

In the specular direction

$$\theta_s = \theta_i \tag{74}$$

$$\langle \overline{E}_s \rangle_v = ik\frac{1}{4\pi R_r}\left(\widehat{v}_s\left(-2R_{v0}\cos\theta_i\right)\right)\exp\left(-2h^2 k_{iz}^2\right)L^2 = \left|\langle \overline{E}_s \rangle_v\right|\exp\left(i\phi_v\right) \tag{75}$$

Thus the phase ϕ_v in the specular direction is given by

$$\phi_v = -\frac{\pi}{2} + phase\left(R_{v0}\right) \tag{76}$$

For horizontal polarized incidence:

$$\widehat{v}_s \cdot \overline{F}(0,0) = 0$$

$$\widehat{h}_s \cdot \overline{F}(0,0) = -2R_{h0}\cos\theta_i$$

In the specular direction

$$\theta_s = \theta_i \tag{77}$$

$$\langle \overline{E}_s \rangle_h = ik\frac{1}{4\pi R_r}\left(\widehat{h}_s\left(-2R_{h0}\cos\theta_i\right)\right)\exp\left(-2h^2k_{iz}^2\right)L^2 = \left|\langle \overline{E}_s \rangle_h\right|\exp\left(i\phi_h\right) \tag{78}$$

The phase is then given by

$$\phi_h = -\frac{\pi}{2} + phase\left(R_{h0}\right) \tag{79}$$

Thus in NMM3D simulations, we first obtain, for vertical polarized incidence, the phase of the wave at specular direction $\theta_s = \theta_i$, ϕ_v. Then the complex amplitude of the coherent wave is

$$E_v^{NMM3D,coh} = \sqrt{r_v^{coh}}\exp\left(i\left(\phi_v + \frac{\pi}{2}\right)\right).$$

Next we obtain, for horizontal polarized incidence, phase of the wave at specular direction $\theta_s = \theta_i$

$$\phi_h.$$

Then the complex amplitude of the coherent wave is

$$E_h^{NMM3D,coh} = \sqrt{r_h^{coh}}\exp\left(i\left(\phi_v + \frac{\pi}{2}\right)\right).$$

In SWC-KA formula, the KA result is replaced by the NMM3D result for unit amplitude RHCP incident wave

$$\left[\left(\widehat{v}_{sn}\widehat{v}_{sn} + \widehat{h}_{sn}\widehat{h}_{sn}\right)\cdot\overline{F}\left(0,0,\alpha_n,\beta_n\right)\right]\exp\left(-\frac{w_n^2h_n^2}{2}\right)$$

$$\rightarrow\quad \left\{-\sqrt{2}\cos\theta_{\ell i}\left[\widehat{v}_{sn}E_v^{NMM3D,coh} + i\widehat{h}_{sn}E_h^{NMM3D,coh}\right]_{NMM3D,\theta_{\ell i}}\right\}$$

Then the coherent scattered wave of NMM3D is

$$E_{sn}^{coh,NMM3D} = \frac{ikE_0}{4\pi R_r}\exp\left(ik\left(R_{nt}+R_{nr}\right)\right)L^2\sec\beta_n\mathrm{sinc}\left(\left(ua_{xx}+va_{yx}\right)\frac{L}{2}\right)\mathrm{sinc}\left(\left(ua_{xy}+va_{yy}\right)\frac{L}{2}\right)$$

$$\left\{\sqrt{2}\cos\theta_{\ell i}\left[\widehat{v}_{sn}E_v^{NMM3D,coh} + i\widehat{h}_{sn}E_h^{NMM3D,coh}\right]_{NMM3D,\theta_{\ell i}}\right\}$$

The SWC power ratio of NMM3D is

$$\frac{P_r^{\mathrm{SWC,NMM3D}}}{P_t} = \frac{G_tG_r}{64\pi^2R_r^2R_t^2}$$

$$\left|\sum_n\exp\left(ik\left(R_{nt}+R_{nr}\right)\right)L^2\sec\beta_n\mathrm{sinc}\left(\left(ua_{xx}+va_{yx}\right)\frac{L}{2}\right)\mathrm{sinc}\left(\left(ua_{xy}+va_{yy}\right)\frac{L}{2}\right)\right.$$

$$\left.\left\{-\sqrt{2}\cos\theta_{\ell i}\left[\widehat{v}_{sn}E_v^{NMM3D,coh} + i\widehat{h}_{sn}E_h^{NMM3D,coh}\right]_{NMM3D,\theta_{\ell i}}\right\}\right|^2$$

5. RADIATIVE TRANSFER (RT) APPROACH FOR LARGER SLOPES

The name "RT" is chosen because in RT theory of volume scattering, the different scatterers are assumed to be independent/uncorrelated. Extending the RT concept to rough surface scattering of patches, it means that the scatterings from different patches are uncorrelated. The RT approach has two distinct features:

(i) The patch phase term $\exp(ik(R_{nt} + R_{nr}))$ is neglected.

(ii) The power ratio depends on the choice of coherent patch size L.

Previously we obtain the RT result for the small slope approximation. In this section, we obtain the result for larger slopes. In mountainous regions, the slopes are much larger than plains. Based on the RT assumption, the power of SWC becomes:

$$\left|\overline{E}_s^{SWC-RT}\right|^2 = \sum_{n=1}^{N}\left|\langle\overline{E}_{sn}\rangle\right|^2 \tag{80}$$

We define the scattering cross section σ_{0n} by

$$\frac{P_r}{P_t} = \frac{G_t G_r \lambda^2}{(4\pi)^3 R_r^2 R_t^2}\sum_{n=1}^{N} A_n\sigma_{0n} \tag{81}$$

where A_n is the area of the nth patch. For SWC-KA-RT,

$$\sigma_{0n}^{SWC-KA-RT} = \frac{\pi}{A_n\lambda^2}\left[\left|\left(\widehat{v_{sn}}\cdot\overline{F}\left(0,0,\alpha_n,\beta_n\right)\right)\right|^2 + \left|\widehat{h_{sn}}\cdot\overline{F}\left(0,0,\alpha_n,\beta_n\right)\right|^2\right]\left|\langle I_{pn}\rangle\right|^2 \tag{82}$$

For SWC-NMM3D

$$\frac{P_r^{SWC-NMM3D-RT}}{P_t}$$

$$= \frac{G_r G_t}{64\pi^2 R_r^2 R_t^2}\sum_n\left|\exp\left(ik\left(R_{nt}+R_{nr}\right)\right)L^2\sec\beta_n\mathrm{sinc}\left((ua_{xx}+va_{yx})\frac{L}{2}\right)\mathrm{sinc}\left((ua_{xy}+va_{yy})\frac{L}{2}\right)\right.$$

$$\left.-\sqrt{2}\cos\theta_i\left[\widehat{v}_{sn}E_v^{NMM3Dcoh}+i\widehat{h}_{sn}E_h^{NMM3Dcoh}\right]\right|^2$$

The SWICI expression remains unchanged because of the inherent incoherent addition of diffuse intensities.

6. NUMERICAL RESULTS

To illustrate the RT results, we further average the SWC and SWICI results over the orientation distributions of the patches. Thus the summation is replaced by an integration $N\int_0^{2\pi}d\alpha\int_0^{\frac{\pi}{2}}d\beta$ over orientation angle.

$$\sum_{n=1}^{N} \rightarrow N\int_0^{2\pi}d\alpha\int_0^{\frac{\pi}{2}}d\beta \tag{83}$$

where $p(\beta,\alpha)$ is the probability density function. We use a uniform slope distribution up to β_u

$$p(\beta,\alpha) = \frac{\sin\beta_u}{2\pi(1-cos\beta_u)} \tag{84}$$

for $0\leq\beta\leq\beta_u$, $0\leq\alpha\leq\pi$.

$\sin\beta$ accounts for the shrinking of the differential solid angle near $\beta=0$. Let A_{eff} be the effective area of DDM pixel.

$$N = A_{eff}/L^2$$

and we use:

$$A_{eff} = 15\,\mathrm{km}\times 15\,\mathrm{km}$$

A typical observed value for power ratio of $15\,\mathrm{km}\times 15\,\mathrm{km}$ effective area is between $-205\,\mathrm{dB}$ and $-175\,\mathrm{dB}$. We choose the following parameters for the DDM area: $G_t = 20$; $Gr = 25$; $h_t = 2.02\times 10^4\,\mathrm{km}$; $h_r = 500\,\mathrm{km}$, $d = 1.74\times 10^4\,\mathrm{km}$ using these parameters, then: $x_s = -x_t = 1.69\times 10^4\,\mathrm{km}$; $x_r = 419.5\,\mathrm{km}$; $\theta_i = 40°$. Since the altitude of the transmitter is much higher than the receiver, the incidence angle θ_i is constant, while the scattered angle θ_s is equal to the incident angle near the specular pint and has significant difference far away from the specular point. For illustration, we choose the patch center to be at $(x_0, y_0, z_0) = (100\,\mathrm{m}, 50\,\mathrm{m}, 10\,\mathrm{m})$: which is close to the specular point.

6.1. Comparisons of SWC-RT and SWICI

In Figure 3, we show the results of SWC-RT and SWICI for $L = 30\,\text{m}$, $N = 2.5 \times 10^5$, $\beta_u = 10°$, $h = 2.5\,\text{cm}$, $l = 20h = 50\,\text{cm}$. Since a much larger slope is used with $\beta_u = 10°$, we used the formula for larger slopes instead of based on the small slope approximation. It is noted that $h = 2.5\,\text{cm}$ is a typical value of rms height used in SMAP [24, 29]. In matching radar backscattering data of UAVSAR [29], $\frac{l}{h}$ is taken between 5 and 50. The results show that SWC-RT is large for small slope and is $-163.7\,\text{dB}$ at $\beta_u \to 0°$. But the value decreases rapidly with increasing in slope. The SWC-RT falls below $-200\,\text{dB}$ at $\beta_u = 8°$. For SWICI, the power ratio is $-188.2\,\text{dB}$ at $\beta_u \to 0°$. It falls much slower than SWC-RT. It becomes larger than SWC-RT at $\beta_u = 3°$. In complex terrain, $30\,\text{m}$ is also too large for a patch to be coherent as there are fine topographical elevations changes. However, the 30 meters is the standard DEM. In Figure 4, we show the results of SWC-RT and SWICI for a smaller patch size of $L = 2\,\text{m}$. The results show that SWC-RT has a much smoother decrease with slope. The power ratio is $-187.2\,\text{dB}$ at $\beta_u \to 0°$. The SWC-RT falls below $-200\,\text{dB}$ at $\beta_u = 8°$. For SWICI, the power ratio is same as that of $L = 30\,\text{m}$ as SWICI is independent of patch size. It becomes larger than SWC-RT at $\beta_u = 3.2°$.
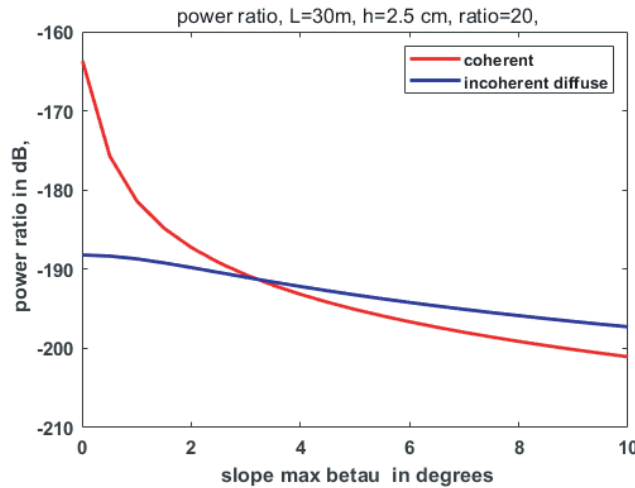
Figure 3. Partially coherent results for $30\,\text{m}$ patch.
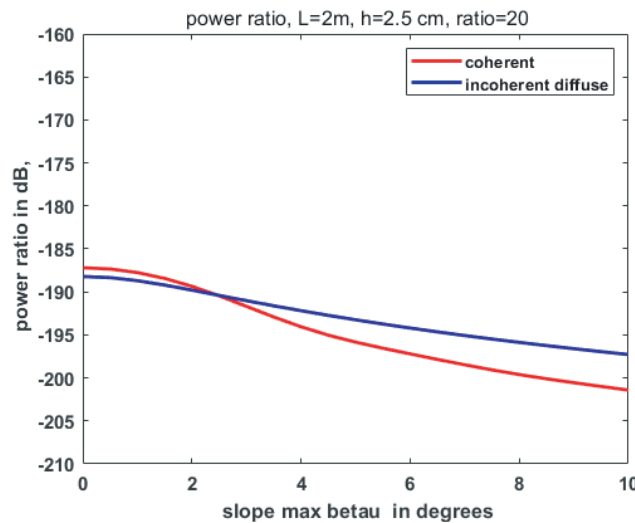
Figure 4. Partially coherent results for $2\,\text{m}$ patch.

6.2. Implementation of Fine-scale Topography $f_2(x, y)$ with Elevation Uncertainties

As described in the introduction section, we consider the surface height as composed of a summation of 3 kinds of roughness/topography.

$$z = f_1(x, y) + f_2(x, y) + f_3(x, y) \tag{85}$$

The coarse scale topography of 30 m in the horizontal plane is represented by $f_3(x, y)$ by linear interpolation. At this moment there is no measurement of fine-scale topography $f_2(x, y)$, thus we are implementing the 3 scale height profile as follows. The $f_3(x, y)$ linear profile of 30 meters is used to decompose into 2 m planar patches. The linear interpolation will give the orientation angle β, α of the patch as well as the x and y slopes of p and q, respectively. The 30 m by 30 m patch is labeled as the "parent" patch as it is decomposed into 225 patches, each of size 2 meters by 2 meters in the horizontal plane. Thus each fine-scale patch n has $L = 2$ m. The 2 meter nth patch has the same slopes p_n and q_n of the "parent" patch. The center of the 2 meter patch is (x_n, y_n, z_n) where x_n, y_n are from the parent patch while z_n is from the original patch with an added gaussian random variable with standard deviation σ. This uncertainty of elevation of gaussian random variable is used to represent $f_2(x, y)$. The normal of the 2 meter patch is in the same direction as the parent 30 meter patch. The normal $\hat{n} = \hat{z}''$ with α, β are the Eulerian angles of the normal. The axes $\hat{x}''$ and $\hat{y}''$ are as described earlier. The microwave roughness is "perpendicular to the patch and is represented by $f_1(x'', y'')$.

Due to the elevation uncertainties, the $\exp(ik(R_{nt} + R_{nr}))$ term gives random phase. By changing the value of σ, the summation of the fields from 2 meter patches can be coherent, incoherent, and partially coherent. We use the same transmitter and receiver setups and the same patch center position in the previous section. In Figure 5, we show the summation of coherent waves from 225 patches of size 2 m by 2 m with same topographical slopes. The results are averaged over 400 realizations for the elevation uncertainties. In Figure 5, the power ratios for 225 2 m patches with $\sigma = 0$ and $\sigma = 3$ cm are shown. For $\sigma = 0$ cm, the power ratio is maximum at $\beta = 0$, and then fluctuate up to 50 dB as the elevation angle β increases. The coherent waves from the 225 patches are adding up fully coherently. The result is the same as a 30 m patch as a whole because of the property of sinc function. For the curve with $\sigma = 3$ cm, the power ratio has a maximum at $\beta = 0$ as well but is smaller than $\sigma = 0$ case, and Pr/Pt decrease smoothly until a dip at 3.5°. With the partially coherent effect, the partially coherent model can match up with data.
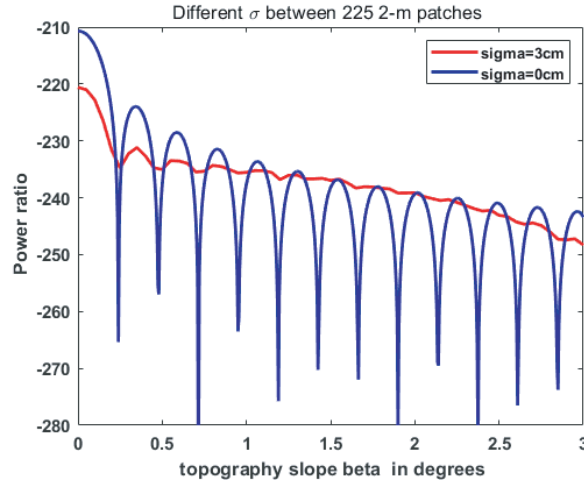
Figure 5. Pr/Pt for 2 m patch with $\sigma = 0$ cm and $\sigma = 3$ cm.

6.3. NMM3D Results

We show the results for the coherent and incoherent Pr/Pt over a 30 m patch near the specular point based on NMM3D. Figure 6 shows the results for the coherent wave contribution from a 30 meter patch
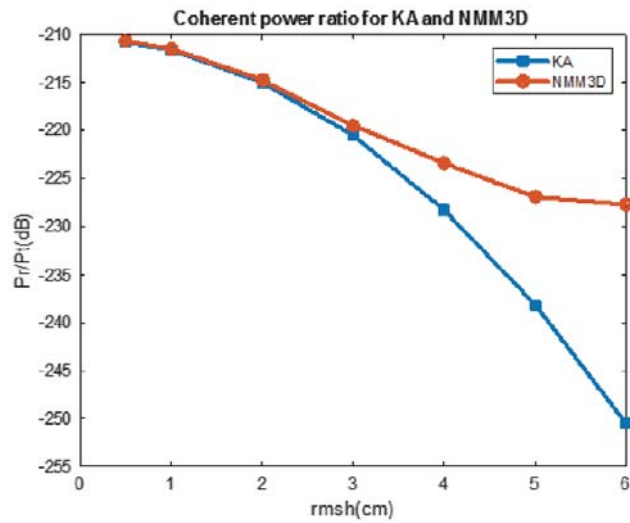
Figure 6. Pr/Pt for 30 m patch with different rms height based on NMM3D and KA.
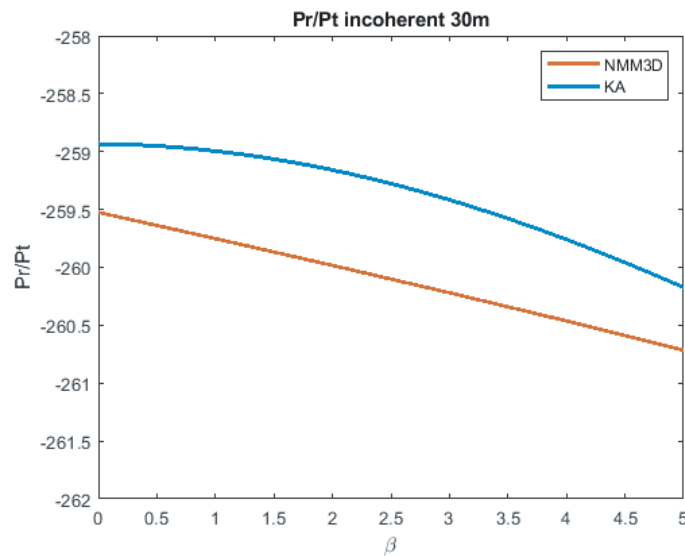
Figure 7. Pr/Pt for 30 m patch with 1 cm rms height with different slope angle.

based on NMM3D results and Kirchhoff. It is shown that the results for NMM3D and KA agree well at small rms height. When the rms height is large, the coherent power form Kirchhoff decays exponentially, while NMM3D results decay much slower. For large rms height, the coherent power still contributes to the total power.

Figure 7 shows the incoherent Pr/Pt for a 30 m patch as a function of slope angle β. The rms height for the rough surface is 1 cm with a correlation length of 10 cm. It is shown that both of the incoherent power curves decrease gradually within 2 dB as the slope angle increases from 0 to 5 degrees. This is because the diffuse scattering pattern is not as directional as the coherent wave scattering. It is well established that Kirchhoff is accurate in the vicinity of the forward direction and becomes inaccurate in the backscattering direction. In particular the VV of KA is inaccurate in radar backscattering such as at 40 degrees incident angle of SMAP.

6.4. DDM Simulation

In the 3-scale roughness and topography of

$$f(x, y) = f_1(x, y) + f_2(x, y) + f_3(x, y) \tag{86}$$

the $f_1(x, y)$ profiles are centimeters microwave roughness which have been measured over CYGNSS sites. The $f_3(x, y)$ profiles are based on coarse scale topography of 30 meters Digital Elevation Model (DEM). We use these DEM data elevations from SRTM mission [30] to construct 30 meters planar patches with slopes to represent $f_3(x, y)$. Each planar patch in $f_3(x, y)$ has a single slope. The $f_2(x, y)$ profiles are a fine scale topography between centimeter microwave roughness and 30 meter coarse scale DEM. The fine scale patch size is L^2. Each L^2 is a fine scale planar patch with microwave roughness $f_1(x, y)$ super imposed on it. The fine scale planar patch L^2 is tilted with slope given by $f_2(x, y) + f_3(x, y)$.

There is presently no available information to characterize fine scale topography. Recently lidar measurements have been taken from which the fine scale topography profiles can be reconstructed in the future. The fine scale topography is important for the fine scale partially coherent patch model because in this intermediate length scale, the scattered waves make transition from coherent to partially coherent and to incoherent. In this paper, we use uncertainties to represent $f_2(x, y)$. The $f_2(x, y)$ generated by uncertainties is shown in Figure 8(b) together with microwave roughness $f_1(x, y)$ in Fig. 8(a) and $f_3(x, y)$ as in Fig. 8(c).

(a)   (b)   (c)
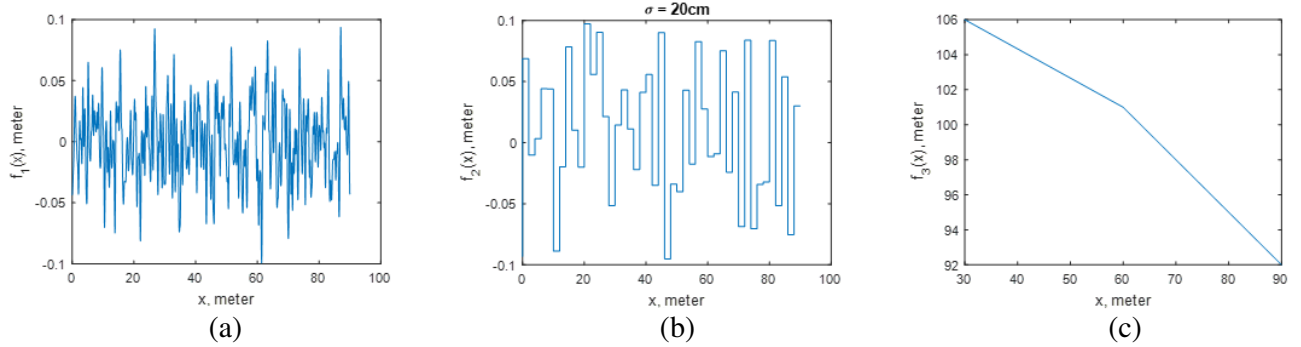
Figure 8. Three scales for the land surface. (a) shows the microwave roughness profile $f_1(x, y)$. $f_1(x, y)$ is the microwave roughness with centimeter scale changes. $f_3(x, y)$ in (c) is the coarse topography in tens of meters scale. $f_2(x, y)$ in (b) is the fine scale topography in the scale of meters. In this paper, we use random variable to represent $f_2(x, y)$ and thus $f_2(x, y)$ are stair cases.

Let A_{DDM} be the physical land area of DDM. In the calculation of complex field summation in Eq. (65), it is not necessary to calculate field summation for the entire DDM area A_{DDM} as in most cases of complex terrain, except water bodies or wetlands, the scattered wave will have become incoherent through addition of complex fields with random phase. This assumption will simplify the implementation of field summations. The DDM area A_{DDM} is divided into large areas of L_{large}^2. L_{large}^2 is chosen so that the scattered wave from L_{large}^2 is incoherent, and intensities summations rather than field summations can be carried out over different L_{large}^2 areas. Within a single L_{large}^2, the scattered wave is assumed to be coherent or partially coherent, so that complex field summation is carried out and then squared to obtain the intensity of that L_{large}^2.

Because of speckle associated with complex field summations, a Monte Carlo approach is taken on the scattered intensities of L_{large}^2 over realizations of $f_2(x, y)$. Let

$$M = \frac{A_{DDM}}{L_{large}^2}$$

be the number of L_{large}^2 in A_{DDM}. Let

$$N_{large} = \frac{L_{large}^2}{L^2}$$

be the number of patches of L^2 in L^2_{large}. With this simplification we then have for the field summation in SWC

$$
\begin{aligned}
\frac{P_r^{SWC}}{P_t} &= \frac{G_r G_t}{64\pi^2 R_r^2 R_t^2} \sum_{m=1}^{M} \left\langle \left| \sum_{n=1}^{N_{large}} L^2 \exp(ik(R_{nt} + R_{nr})) \exp(-2k^2 h_n^2 \cos^2 \theta_i) \mathrm{sinc}\left(\frac{(k_{dmx} + k_{dmz}p_n)L}{2} \right) \right. \right. \\
&\quad \left. \left. \mathrm{sinc}\left(\frac{(k_{dmy} + k_{dmz}q_n)L}{2} \right) \left[\frac{2\cos\theta_i[\hat{v}_s R_v(\theta_i) + i\hat{h}_s R_h(\theta_i)]}{\sqrt{2}} \right] \right|^2 \right\rangle_m
\end{aligned} \tag{87}
$$

where we use the mth index for L^2_{large} and the nth index for L^2. The angular bracket $\langle \rangle_m$ denotes averaging over realizations of fine scale topography $f_2(x, y)$ over the single mth L^2_{large}. The n index denotes the nth L^2 patch inside the mth L^2_{large}. The choices of L and L_{large} are dependent on terrain and are subjects of continued studies. In this paper we choose

$$L = 2m$$
$$L_{large} = 30m$$
$$N_{large} = 225$$

In DDM simulations, a weighting factor is inserted that represents the discretization of the very large DDM area based on delay-doppler signal processing.

Let

$$P_{ij} = \frac{P_r}{P_t}$$

of the i, jth pixel in the DDM.

We follow the formulations in [15]. Then

$$
\begin{aligned}
\frac{P_{rij}^{SWC}}{P_t} &= \frac{G_r G_t}{64\pi^2 R_r^2 R_t^2} \sum_{m=1}^{M} |W_m(i, j)|^2 \\
&\quad \left\langle \left| \sum_{n=1}^{N} \exp(ik(R_{nr} + R_{nt})) \left(\widehat{v}_{sn}\left(\widehat{v}_{sn} \cdot \overline{F}(0, 0, \alpha_n, \beta_n) \right) + \widehat{h}_{sn} \left(\widehat{h}_{sn} \cdot \overline{F}(0, 0, \alpha_n, \beta_n) \right) \right) \langle I_{pn} \rangle \right|^2 \right\rangle_m
\end{aligned} \tag{88}
$$

Figure 9. Location of Cal/Val site sensors and DDM Specular points. The data near Z1 is taken from CYGNSS v2.1 data, and the data near Z4 is from CYGNSS sandbox data. Both are from day 301 of 2019.

We truncate the coherent summation of fields over $2\,\text{m}$ patches at $N = 225$ which is at $30\,\text{m} \times 30\,\text{m}$ area size, that is within $30\,\text{m} \times 30\,\text{m}$, we add up the fields while between $30\,\text{m} \times 30\,\text{m}$, the intensities are added up. The index m is for the $30\,\text{m} \times 30\,\text{m}$ areas, and we have M $30\,\text{m} \times 30\,\text{m}$ areas contributing to the ith delay, jth doppler bin. The incoherent part is expressed as

$$\frac{Pr^{SWCICI}}{Pt}$$

$$= \frac{G_r G_t}{64\pi^2 R_r^2 R_t^2} \sum_{n=1}^{N} |W_n(i,j)|^2 \left(\left| \widehat{v}_{sn} \cdot \overline{F}(0,0,\alpha_n,\beta_n) \right|^2 + \left| \widehat{h}_{sn} \cdot \overline{F}(0,0,\alpha_n,\beta_n) \right|^2 \right) \left\langle |I_p - \langle I_p \rangle|^2 \right\rangle_n \quad (89)$$

In simulating the DDMs, we use a coherent patch size of $2\,\text{m}$. The topographical elevations and slopes are obtained by SRTM data with $30\,\text{m}$ resolution [30].

We compare the simulation results with CYGNSS data. Ground Cal/Val measurements have performed at San Luis valley sites, and soil moisture sensors are planted at sites Z1 and Z4 as shown
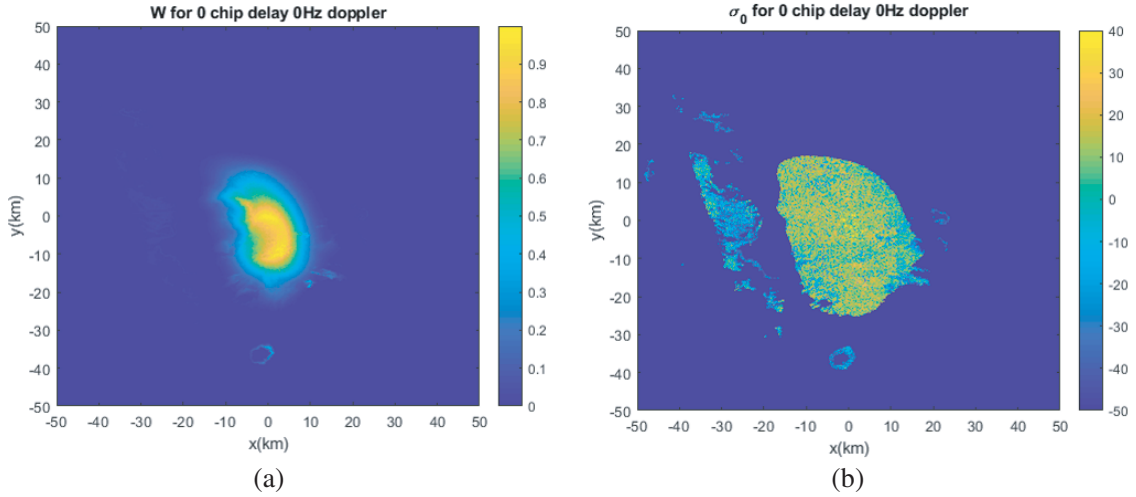
Figure 10. Weighting function for 0 chip delay and $0\,\text{Hz}$ doppler pixel in (a) DDM and (b) normalized bistatic RCS σ_0. The σ_0 is shown for area where weighting function value $|W|^2 > 0.01$.
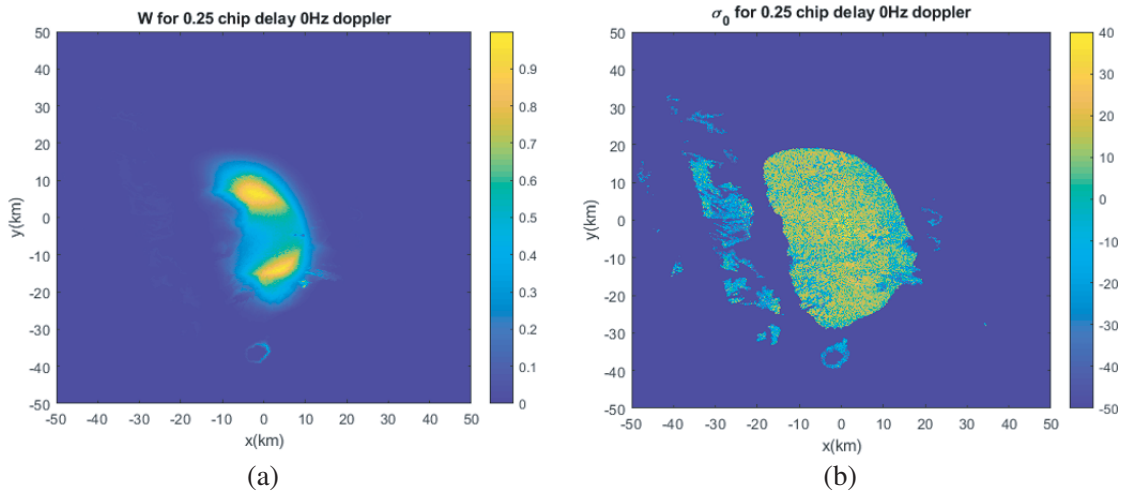
Figure 11. Weighting function for 0.25 chip delay and $0\,\text{Hz}$ doppler pixel in (a) DDM and (b) normalized bistatic RCS σ_0. The σ_0 is shown for area where weighting function value $|W|^2 > 0.01$.
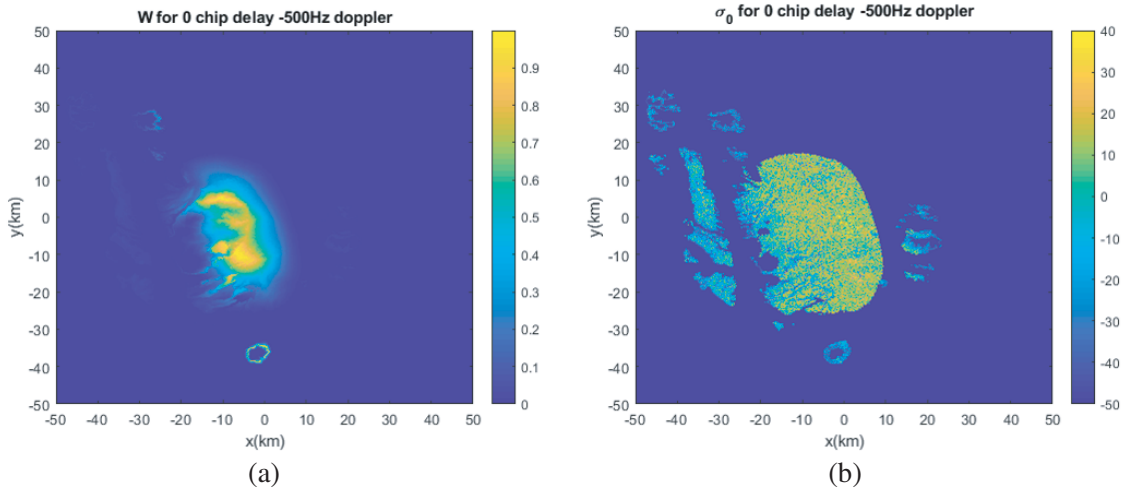
Figure 12. Weighting function for 0 chip delay and $-500\,\mathrm{Hz}$ doppler pixel in (a) DDM and (b) normalized bistatic RCS σ_0. The σ_0 is shown for area where weighting function value $|W|^2 > 0.01$.
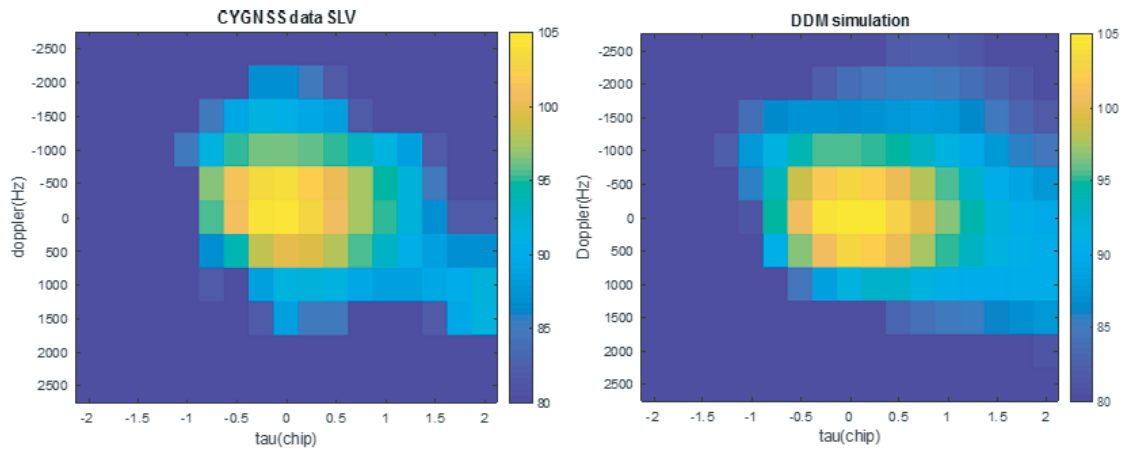
Figure 13. DDM simulation compared with data in σ_{brcs} at the site close to Z1. The σ_{brcs} is plotted in dB square meter.

in Figure 9. Since the soil moisture data have not been calibrated, we assume the soil permittivity be $5.5 + 2i$, which is about 10 percent soil moisture. We choose 2 DDMs: one is at plain area (Lat: $37.197\,\mathrm{N}$ Lon: $106.0032\,\mathrm{W}$) near the senors of Z1, and the other ($37.077\,\mathrm{N}$ $105.8332\,\mathrm{W}$) is in mountainous area near Z4.

Through Figure 10 to Figure 12, we show the weighting function $|W|^2$ map for the bins of tau $= 0\,\mathrm{chip}$, doppler $= 0\,\mathrm{Hz}$, tua $= 0.25\,\mathrm{chip}$ doppler $= 0\,\mathrm{Hz}$ and tau $= 0\,\mathrm{chip}$, doppler $= -500\,\mathrm{Hz}$. The detailed expression for weighing function can be found in appendix. The weighting function value is shown on the left column while the normalized bistatic cross section (σ_0) is shown on the right. We show σ_0 for the area where $|W|^2 > 0.01$. By observing the changes in delay and doppler respectively, we see that as the delay increases, the peak value of weighing function moves away from specular point, and as the doppler frequency decreases, the peak value moves to the left.

Figure 13 shows the comparison of data and simulation. We use $2\,\mathrm{cm}$ uncertainty as f_2 for flat area and $3\,\mathrm{cm}$ uncertainty for mountainous area and rms heights of $0.5\,\mathrm{cm}$ and $2.5\,\mathrm{cm}$, respectively. Due to the flatness of the region, the scattered power has more coherent effect, which means that the area near the specular point will contribute more scattered power. As in the DDMs, the pixels close to 0 delay 0 doppler bins should be much greater than other pixels. This is observed in the CYGNSS data
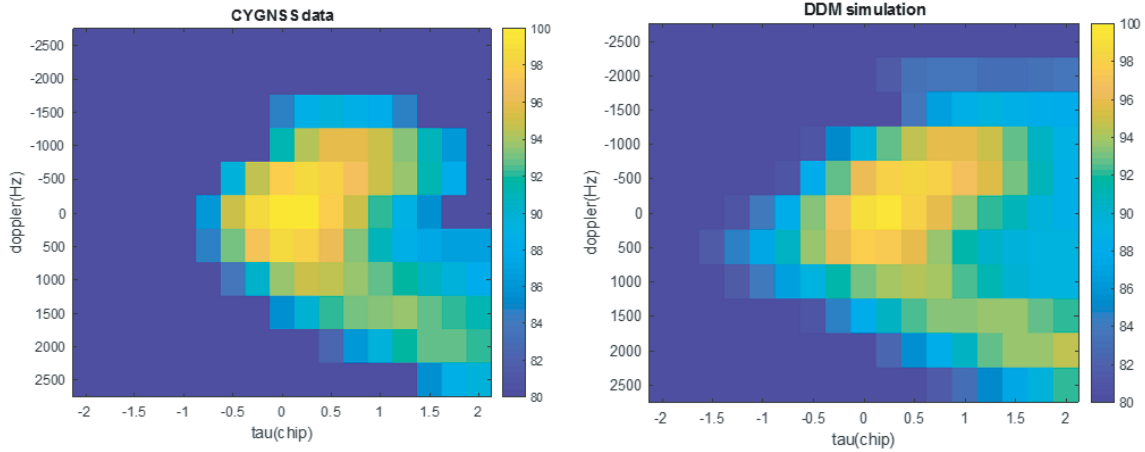
Figure 14. DDM simulation compared with data in the format of σ_{brcs} close to Z4. The σ_{brcs} is plotted in dB square meter.

which has a bistatic radar cross section of 104.5 dBsm. The simulated DDM also shows a peak in the center and has a center pixel value of 106 dBsm. In Figure 14, the power in DDM bins are more spread out. This is because the specular point is close to mountainous area, where coherent effect is low due to the land variations. We use 4 cm uncertainty to represent the variation of f_2 in mountainous region and use 3 cm uncertainty in the plain area. The rms heights for 2 regions are selected as 0.5 cm and 2.5 cm, respectively. The center pixel is 98.95 dBsm from simulation, and the data have a peak value of 100.5 dBsm. The asymmetry of the DDM is because negative doppler bins have more flat area than the positive doppler bins.

7. CONCLUSION

In this paper, we present a fine scale partially coherent patch model for GNSS-R land application. The complex terrain is assumed to be composed of three scales of roughness and topography. In the 3-scale roughness/topography of $f(x, y) = f_1(x, y) + f_2(x, y) + f_3(x, y)$, the $f_1(x, y)$ profiles are centimeters microwave roughness which have been measured in CYGNSS sites. The $f_3(x, y)$ profiles are based on coarse scale topography of 30 meters Digital Elevation Model (DEM). The intermediate scale $f_2(x, y)$ is important for this partially coherent model as the scattered waves make transitions from coherent to partially coherent and to incoherent in this length scale. Complex field summations are used within area of L_{large}^2, and intensity summations are used over areas of L_{large}^2. The simulated DDMs are in good agreement with CYGNSS data. In the present version of the fine scale partially coherent patch model, we use uncertainties of gaussian random variables to characterize $f_2(x, y)$. The characterization of $f_2(x, y)$ is a subject of continued studies and will be related to recent lidar measurements of complex terrain. The characterization of $f_2(x, y)$ profiles from lidar measurements will be used to develop a new version of FPCP.

APPENDIX A. NMM3D DIFFUSE Γ

In this appendix we describe the derivation of the $\overline{\overline{\Gamma}}^{NMM3D, dif}$ from the NMM3D simulation data.

For each realization, we have a unit amplitude incident vertically polarized wave $E_{v_\ell}^i = 1$ from which the scattered amplitudes of $E_{v_\ell}^s$ and $E_{h_\ell}^s$ are calculated. Then the scattering amplitudes $f_{v_\ell v_\ell}$ and $f_{h_\ell v_\ell}$ are derived.

This is repeated for horizontal polarized incidence $E_{h_\ell}^i = 1$, from which $f_{v_\ell h_\ell}$ and $f_{h_\ell h_\ell}$ are derived.

The scattering amplitudes, $f_{v_\ell v_\ell}$, $f_{h_\ell v_\ell}$, $f_{v_\ell h_\ell}$ and $f_{h_\ell h_\ell}$, are normalized such that the bistatic scattering coefficients of the incoherent waves are calculated.

For general $E^i_{v_\ell}$ and $E^i_{h_\ell}$,

$$E^s_{v_\ell} = \frac{1}{R_r}\left(f_{v_\ell v_\ell}E^i_{v_\ell} + f_{v_\ell h_\ell}E^i_{h_\ell}\right)$$

$$E^s_{h_\ell} = \frac{1}{R_r}\left(f_{h_\ell v_\ell}E^i_{v_\ell} + f_{h_\ell h_\ell}E^i_{h_\ell}\right)$$

Thus we have the relations similar to the phase matrix of page 125 of [12]. Using the simulation data for each realization, averages are taken, and the coherent waves are subtracted to obtain the diffuse incoherent waves.

$$\begin{bmatrix} \left|E^s_{v_\ell}\right|^2 \\ \left|E^s_{h_\ell}\right|^2 \\ E^s_{v_\ell}E^{s*}_{h_\ell} \\ E^{s*}_{v_\ell}E^s_{h_\ell} \end{bmatrix}_{dif} = \frac{1}{R_r^2}\begin{bmatrix} \left|f_{v_\ell v_\ell}\right|^2 & \left|f_{v_\ell h_\ell}\right|^2 & f_{v_\ell v_\ell}f^*_{v_\ell h_\ell} & f^*_{v_\ell v_\ell}f_{v_\ell h_\ell} \\ \left|f_{v_h v_\ell}\right|^2 & \left|f_{h_\ell h_\ell}\right|^2 & f_{h_\ell v_\ell}f^*_{h_\ell h_\ell} & f^*_{h_\ell v_\ell}f_{h_\ell h_\ell} \\ f_{v_\ell v_\ell}f^*_{h_\ell v_\ell} & f_{v_\ell h_\ell}f^*_{h_\ell h_\ell} & f_{v_\ell v_\ell}f^*_{h_\ell h_\ell} & f_{v_\ell h_\ell}f^*_{h_\ell v_\ell} \\ f^*_{v_\ell v_\ell}f_{h_\ell v_\ell} & f^*_{v_\ell h_\ell}f_{h_\ell h_\ell} & f^*_{v_\ell h_\ell}f_{h_\ell v_\ell} & f^*_{v_\ell v_\ell}f_{h_\ell h_\ell} \end{bmatrix}_{dif}\begin{bmatrix} \left|E^i_{v_\ell}\right|^2 \\ \left|E^i_{h_\ell}\right|^2 \\ E^i_{v_\ell}E^{i*}_{h_\ell} \\ E^{i*}_{v_\ell}E^i_{h_\ell} \end{bmatrix}$$

where "dif" denotes the diffuse incoherent waves. Using definitions of bistatic scattering coefficients.

$$\gamma_{\chi_\ell \kappa_\ell} = \frac{4\pi R_r^2 \left|E^s_{\chi_\ell}\right|^2}{\left|E^i_{\kappa_\ell}\right|^2 A_P \cos\theta_{\ell i}} = \frac{4\pi \left|\gamma_{\chi_\ell \kappa_\ell}\right|^2}{\left|E^i_{\alpha_\ell}\right|^2 A_P \cos\theta_{\ell i}}$$

the $\Gamma^{NMM3D,dif}(\theta_{\ell s}, \phi_{\ell s} - \phi_{\ell i}, \theta_{\ell i}, 0)$ is defined by

$$\Gamma(\theta_{\ell s}, \phi_{\ell s} - \phi_{\ell i}, \theta_{\ell i}, 0) = \frac{4\pi}{A_P \cos\theta_{\ell i}}\begin{bmatrix} \left|f_{v_\ell v_\ell}\right|^2 & \left|f_{v_\ell h_\ell}\right|^2 & f_{v_\ell v_\ell}f^*_{v_\ell h_\ell} & f^*_{v_\ell v_\ell}f_{v_\ell h_\ell} \\ \left|f_{v_h v_\ell}\right|^2 & \left|f_{h_\ell h_\ell}\right|^2 & f_{h_\ell v_\ell}f^*_{h_\ell h_\ell} & f^*_{h_\ell v_\ell}f_{h_\ell h_\ell} \\ f_{v_\ell v_\ell}f^*_{h_\ell v_\ell} & f_{v_\ell h_\ell}f^*_{h_\ell h_\ell} & f_{v_\ell v_\ell}f^*_{h_\ell h_\ell} & f_{v_\ell h_\ell}f^*_{h_\ell v_\ell} \\ f^*_{v_\ell v_\ell}f_{h_\ell v_\ell} & f^*_{v_\ell h_\ell}f_{h_\ell h_\ell} & f^*_{v_\ell h_\ell}f_{h_\ell v_\ell} & f^*_{v_\ell v_\ell}f_{h_\ell h_\ell} \end{bmatrix}_{dif}$$

$$= \begin{bmatrix} \gamma^\ell_{11} & \gamma^\ell_{12} & \gamma^\ell_{13} & \gamma^\ell_{14} \\ \gamma^\ell_{21} & \gamma^\ell_{22} & \gamma^\ell_{23} & \gamma^\ell_{24} \\ \gamma^\ell_{31} & \gamma^\ell_{32} & \gamma^\ell_{33} & \gamma^\ell_{34} \\ \gamma^\ell_{41} & \gamma^\ell_{42} & \gamma^\ell_{43} & \gamma^\ell_{44} \end{bmatrix}_{incoh} (\theta_{\ell s}, \phi_{\ell s} - \phi_{\ell i}, \theta_{\ell i}, 0)$$

The relation is used in deriving the SWICI of NMM3D.

APPENDIX B. GEOMETRIC OPTICS APPLIED TO SWC-RT

In this appendix, we apply the geometric optics to the SWC-RT approach, getting equations for power ratio labeled as "SWC-RT-GO". In geometric optics, wavenumber k is large. For the patch model, this means that the patch size L is such that $kL \gg 1$. However, the microwave roughness rms height h can still be small compared with wavelength. In this derivation, we take 2 approximations of the sinc^2 function.

Consider that the function $\lim_{\epsilon_d \to 0}\frac{1}{\pi\epsilon_d}\text{sinc}^2(\frac{x}{\epsilon_d})$ is a sharply peaked positive function. It is similar to a dirac delta function. To approximate by a delta function, we also equate the integral as the integration of dirac delta function is equal to unity:

The first approximation is replaced by a delta function

$$\lim_{\epsilon_d \to 0}\frac{1}{\pi\epsilon_d}\text{sinc}^2\left(\frac{x}{\epsilon_d}\right) = \delta(x) \tag{B1}$$

The second approximation is replaced by a gaussian function

$$\lim_{\epsilon_d \to 0}\frac{1}{\pi\epsilon_d}\text{sinc}^2\left(\frac{x}{\epsilon_d}\right) = \lim_{\epsilon_d \to 0}\frac{1}{\pi\epsilon_d}\exp\left(-\frac{1}{\pi}(\frac{x}{\epsilon_d})^2\right) \tag{B2}$$

Note that we match the integral of the function rather than the quadratic dependence at the origin. An examination of the quadratic dependence at $x = 0$ has a small difference with 3 on the left handside and π on the right handside.

B.1. Approximation of Replacing sinc^2 by Delta Functions

For large patch size L, we have the following approximation, using $\epsilon_d = \frac{2}{k_{dnz}L}$:

$$\text{sinc}^2\left(\left(\frac{k_{dnx}}{k_{dnx}} + p_n\right)\frac{k_{dnz}L}{2}\right)\text{sinc}^2\left(\left(\frac{k_{dny}}{k_{dnz}} + q_n\right)\frac{k_{dnz}L}{2}\right) = \frac{4\pi^2}{k_{dnz}^2 L^2}\delta\left(\frac{k_{dnx}}{k_{dnx}} + p_n\right)\delta\left(\frac{k_{dny}}{k_{dnz}} + q_n\right)$$
(B3)

We further use $k_{dnz}^2 = 4k^2\cos^2\theta_i$. Then the power ratio is

$$\frac{P_r^{\text{SWC-RT}}}{P_t} = \frac{G_r G_t \lambda^2}{64\pi^2 R_r^2 R_t^2}\sum_{n=1}^{N} L^2 e^{-4k^2 h_n^2 \cos^2\theta_i}\left|R_{CP}\left(\theta_{in}\right)\right|^2 \delta\left(\frac{k_{dnx}}{k_{dnx}} + p_n\right)\delta\left(\frac{k_{dny}}{k_{dnz}} + q_n\right)$$
(B4)

where h_n is the rms height of microwave roughness, and θ_{in} is the incident angle on the nth patch.

We next carry an average over the topographical slope distributions. Let $p_T(p, q)$ be the probability density function of the topography slope. Then integrating by $\int_{-\infty}^{\infty} dp \int_{-\infty}^{\infty} dq p_T(p, q)$ over the dirac delta functions,

$$\frac{P_r^{\text{SWC-RT}}}{P_t} = \frac{G_r G_t \lambda^2}{64\pi^2 R_r^2 R_t^2}\sum_{n=1}^{N} L^2 e^{-4k^2 h_n^2 \cos^2\theta_i}\left|R_{CP}\left(\theta_{in}\right)\right|^2 p_T\left(p = -\frac{k_{dnx}}{k_{dnx}}, q = \frac{k_{dny}}{k_{dnz}}\right)$$
(B5)

The above is identical to Zavoronty's [15] work.

For homogeneous terrain and close to the specular point, we drop the n term and set $\theta_{sn} = \theta_{in} = \theta_i$. The formula then is simplified to:

$$\frac{P_r^{\text{SWC-RT-GO}}}{P_t} = \frac{G_r G_t \lambda^2 A}{64\pi^2 R_r^2 R_t^2} e^{-4k^2 h^2 \cos^2\theta_i}\left|R_{CP}\left(\theta_i\right)\right|^2 p_T\left(p = 0, q = 0\right)$$
(B6)

where A is the area. Consider the example of Gaussian distribution of topographical slope

$$p_T(p, q) = \frac{1}{2\pi s_T^2}\exp\left(-\frac{p^2 + q^2}{2s_T^2}\right)$$
(B7)

where the parameter s_T denotes the topographical slope, then we have:

$$\frac{P_r^{\text{SWC-RT-GO}}}{P_t} = \frac{G_r G_t \lambda^2 A}{64\pi^2 R_r^2 R_t^2}\left(\frac{1}{2\pi s_T^2}\right)e^{-4k^2 h^2 \cos^2\theta_i}\left|R_{CP}\left(\theta_i\right)\right|^2$$
(B8)

which coincides, aside from the factor $\exp(-4k^2 h^2 \cos^2\theta_i)$, with the incoherent model [14].

In Figure B1, we plot the case using the SWC-RT formula versus the simple formula with different patch sizes for the SWC-RT. We let

$$L = 1, 2, 10, 30\,\text{meters}$$

and set the rms height $h = 0$.

We see that the case of $L = 10\,\text{m}$ has a small difference from geometric optics while the case of $L = 30\,\text{m}$ becomes identical with that of geometrical optics. The cases of $L = 1$ meter and $L = 2$ meters have significant differences from that of the incoherent model.

B.2. Approximation of Replacing sinc^2 by Gaussian Functions

Using $\epsilon_d = \frac{2}{k_{dnz}L}$, then

$$\text{sinc}^2\left(\left(\frac{k_{dnx}}{k_{dnx}} + p_n\right)\frac{k_{dnz}L}{2}\right)\text{sinc}^2\left(\left(\frac{k_{dny}}{k_{dnz}} + q_n\right)\frac{k_{dnz}L}{2}\right)$$
$$= \exp\left(-\frac{k_{dnz}^2 L^2}{4\pi}\left[\left(\frac{k_{dnx}}{k_{dnx}} + p_n\right)^2 + \left(\frac{k_{dny}}{k_{dnx}} + q_n\right)^2\right]\right)$$
(B9)
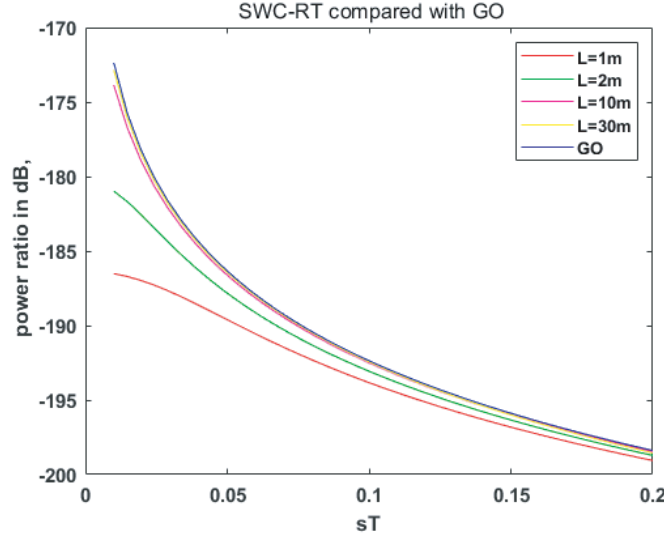
Figure B1. Pr/Pt for different patch size.

We further use $k_{dnz}^2 = 4k^2 \cos^2 \theta_i$. Then the power ratio is

$$\frac{P_r^{SWC-RT}}{P_t} = \frac{G_r G_t \lambda^2}{64\pi^2 R_r^2 R_t^2} \sum_{n=1}^{N} L^2 |R_{CP}(\theta_i)|^2 \frac{k^2 L^2 \cos^2 \theta_i}{\pi^2}$$

$$\exp\left(-\frac{k^2 \cos^2 \theta_i L^2}{\pi}\left[\left(\frac{k_{dnx}}{k_{dnx}} + p_n\right)^2 + \left(\frac{k_{dny}}{k_{dnx}} + q_n\right)^2\right]\right) e^{-4k^2 h_n^2 \cos^2 \theta_i}$$

We define the cross section σ_{0n} such that:

$$\frac{P_r^{\text{SWC-KA-RT}}}{P_t} = \frac{G_r G_t \lambda^2}{64\pi^2 R_r^2 R_t^2} \sum_{n=1}^{N} L^2 \frac{\sigma_{0n}}{\pi} \tag{B10}$$

Then

$$\sigma_{0n} = |R_{CP}(\theta_i)|^2 \frac{k^2 L^2 \cos^2 \theta_i}{\pi}$$

$$\exp\left(-\frac{k^2 \cos^2 \theta_i L^2}{\pi}\left[\left(\frac{k_{dnx}}{k_{dnx}} + p_n\right)^2 + \left(\frac{k_{dny}}{k_{dnx}} + q_n\right)^2\right]\right) e^{-4k^2 h_n^2 \cos^2 \theta_i}$$

If we let $\frac{(k \cos \theta_i L)^2}{\pi} = \frac{1}{2\sigma_{rg}^2}$, the above formula is the same as Equations (46) and (47) in [17]. The three incoherent optics models: Mohammad, Zavotnony, and Campbell based on geometric optics are of similar concepts. The differences among the three models are the evaluations of the slope probability. The incoherent model in [14] evaluates the value at zero slope in both x and y directions. In paper [15], the value is evaluated considering the difference between the incident and scattering direction that is far away from the specular point. Campbell's model evaluates the values at the topographical slope together with difference between the incident and scattering angle.

APPENDIX C. WEIGHTING FUNCTION FOR DDMS

In this section, we show the definition of weighting functions as given in [15]. The received signal is given as:

$$u(t) = \sum_{n=1}^{N} \sqrt{A_e} u_n a(t - \tau_n]) \exp\left(-2\pi i f_n^{doppler} t\right) \tag{C1}$$

where A_e is the effective aperture of the receiver antenna, $a(t - \tau_n)$ the PRN code from the GPS satellite, and $tau_n = [R_{nt} + R_{nr}/c0$ the delay from nth patch. $f_n^{doppler} = (\overline{v}_t \cdot \widehat{R}_n t - \overline{v}_r \cdot \widehat{R}_r s)/\lambda$ is the doppler frequency of the nth patch. To get the power for each delay and doppler bin, the signal is correlated with reference PRN code and frequency signal.

$$Y(\tau_i, f_j) = \int_0^{T_i} a(t)u(t) \exp(2\pi i f_j t) dt \tag{C2}$$

where T_i is the integration time and usually much greater than τ_c, which is the chip length. Then

$$Y(\tau_i, f_j) = T_i \sum_{n=1}^{N} u_n \frac{1}{T_i} \int_0^{T_i} a(t)a(t - \tau_n) \exp\left(-2\pi i \left(f_n^{doppler} - f_j\right)\right) \tag{C3}$$

and the term

$$\chi(\delta\tau, \delta f) = \frac{1}{T_i} \int_0^{T_i} a(t)a(t + \delta\tau) \exp(-2\pi i (\delta f)) \tag{C4}$$

is known as the Woodward Ambiguity Function and can be approximated as

$$\chi(\delta\tau, \delta f) = \Lambda(\delta\tau)S(\delta f) \tag{C5}$$

where $\Lambda(\delta\tau)$ and $S(\delta f)$ are weighting functions in the delay and doppler domain, respectively:

$$\Lambda(\delta\tau) = \frac{1}{T_i} \int_0^{T_i} a(t)a(t + \delta\tau) dt \tag{C6}$$

$$= 1 - \frac{\delta\tau}{T_i}, |\delta\tau| \leq \tau_c(1 - \tau_c/T_i) \tag{C7}$$

$$= -\tau_c/T_i, |\delta\tau| \geq \tau_c(1 - \tau_c/T_i) \tag{C8}$$

since T_i is much larger than τ_c, $-\tau_c/T_i = 0$. For the weighting function in frequency domain, we have

$$S(\delta f) = \frac{1}{T_i} \int_0^{Ti} \exp(-2\pi i \delta f t) dt = \frac{\sin(\pi\delta f T_i)}{\pi\delta f T_i} \exp(-\pi i \delta f T_i) \tag{C9}$$

The weighting function on each patch is thus defined as:

$$W_n(i, j) = \Lambda(\tau_n - \tau_i)S\left(f_n^{doppler} - f_j\right) \tag{C10}$$

REFERENCES

1. Unwin, M., P. Jales, J. Tye, C. Gommenginger, G. Foti, and J. Rosello, "Spaceborne GNSS-reflectometry on TechDemoSat-1: Early mission operations and exploration," *IEEE JASTARS*, Vol. 9, No. 10, 4525–4539, Oct. 2016.

2. Ruf, C., et al., "CYGNSS: Enabling the future of hurricane prediction," *IEEE Geosci. Remote Sens. Mag.*, Vol. 1, No. 2, 52–67, 2013.

3. Clarizia, M. P. and C. S. Ruf, "Wind speed retrieval algorithm for the Cyclone Global Navigation Satellite System (CYGNSS) mission," *IEEE Transactions on Geoscience and Remote Sensing*, Vol. 54, No. 8, 4419–4432, 2016.

4. Li, W., E. Cardellach, F. Fabra, A. Rius, S. Ribo, and M. Martin-Neira, "First spaceborne phase altimetry over sea ice using TechDemosat-1 GNSS-R signals," *Geophysical Research Letters*, Vol. 44, 8369–8376, 2017.

5. Nghiem, S. V., C. Zfuffada, R. Shah, C. Chew, et al., "Wetland monitoring with Global Navigation Satellite System reflectometry," *Earth and Space Science*, Vol. 4, No. 1, 16–39, 2017.

6. Kim, H. and V. Lakshmi, "Use of Cyclone Global Navigation Satellite System (CyGNSS) observations for estimation of soil moisture," *Geophysical Research Letters*, Vol. 45, No. 16, 8272–8282, Aug. 2018.

7. Chew, C. C. and E. E. Small, "Soil moisture sensing using spaceborne GNSS reflections: Comparison of CYGNSS reflectivity to SMAP soil moisture," *Geophysical Research Letters*, Vol. 45, 4049–4057, 2018.

8. Clarizia, M. P., N. Pierdicca, F. Costantini, and N. Floury, "Analysis of CYGNSS data for soil moisture retrieval," *IEEE J. Sel. Topics Appl. Earth Observ. Remote Sens.*, Vol. 12, No. 7, 2227–2235, Jul. 2019.

9. Beckmann, P. and A. Spizzichino, *The Scattering of Electromagnetic Waves from Rough Surfaces*, Macmillan, New York, 1963.

10. Gu, W., H. Xu, and L. Tsang, "A numerical Kirchhoff simulator for GNSS land applications," *Progress In Electromagnetics Research*, Vol. 164, 119–133, 2019.

11. Bertoni, H., *Radio Propagation for Modern Wireless Systems*, Prentice Hall, 1999.

12. Tsang, L., J. Kong, and K. Ding, *Scattering of Electromagnetic Waves, Vol. 1: Theory and Applications*, Wieley Interscience, New York, 2000.

13. Tsang, L., J. Kong, and K. Ding, *Scattering of Electromagnetic Waves, Vol. 3: Advanced Topics*, Wieley Interscience, New York, 2000.

14. Al-Khaldi, M. M., J. T. Johnson, A. J. O'Brien, A. Balenzano, and F. Mattia, "Time series retrieval of soil moisture using CYGNSS," *IEEE Transcations on Geoscience and Remote Sensing*, Vol. 57, No. 7, Jul. 2019.

15. Zavorotny, V. and A. Voronovich, "Scattering of GPS signals form the ocean with wind remote sensing application," *IEEE Transactions on Geoscience and Remote Sensing*, Vol. 38, No. 2, 951–964, Mar. 2000.

16. Campbell, J. D., A. Melebari, and M. Moghaddam, "Modeling the effects of topography on delay-doppler maps," *IEEE Journal of Selected Topics in Applied Earth Observations and Remote Sensing*, Vol. 13, 1740–1751, 2020.

17. Campbell, J. D., A. Melebari, and M. Moghaddam, "Land forward model matchups with CYGNSS observations in the presence of topography," *CYGNSS Science Team Meeting*, Ann Arbor, Jun. 2019.

18. Dente, L., L. Guerriero, D. Comite and N. Pierdicca, "Space-borne GNSS-R signal over a complex topography: Modeling and validation," *IEEE Journal of Selected Topics in Applied Earth Observations and Remote Sensing*, Vol. 13, 1218–1233, 2020.

19. Zhu, J.-Y., L. Tsang and H. Xu, "A physical patch model for GNSS-R land applications," *Progress In Electromagnetic Research*, Vol. 165, 93–105, 2019.

20. Al-Khaldi, M. M., J. T. Johnson, S. Gleason, E. Loria, A. J. O'Brien, and Y. Yi, "An algorithm for detecting coherence in cyclone global navigation satellite system mission level-1 delay-doppler maps," *IEEE Transactions on Geoscience and Remote Sensing*, 1–10, 2020, Early Access.

21. Bringer, A., C. Toth, and J. T. Johnson, "Land Cal/Val activities: LIDAR campaign update," *CYGNSS Science Team Meeting*, Ann Arbor, Jun. 2019.

22. Oh, Y., K. Sarabandi, and F. T. Ulaby, "An empirical model and an inversion technique for radar scattering from bare soil surfaces," *IEEE Transactions on Geoscience and Remote Sensing*, Vol. 30, No. 2, 370–381, Mar. 1992.

23. Huang, S., L. Tsang, E. G. Njoku, and K. S. Chan, "Backscattering coefficients, coherent reflectivities, and emissivities of randomly rough soil surfaces at L-band for SMAP applications based on numerical solutions of Maxwell Equations in three-dimensional simulations," *IEEE Transactions on Geoscience and Remote Sensing*, Vol. 48, No. 6, 2557–2568, Jun. 2010.

24. Entekhabi, D., E. G. Njoku, P. E. O. Neill, K. H. Kellogg, W. T. Crow, W. N. Edelstein, et al., "The Soil Moisture Active Passive (SMAP) mission," *Proceedings of the IEEE*, Vol. 98, No. 5, 704–716, 2010.

25. Huang, H., S.-B. Kim, L. Tsang, X. Xu, T.-H. Liao, T. J. Jackson, and S. Yueh, "Coherent model of L-band radar scattering by soybean plants: Model development, validation and retrieval," *IEEE J. Sel. Topics Appl. Earth Observ. Remote Sens.*, Vol. 9, No. 1, 272–284, Jan. 2015.

26. Huang, H., T.-H. Liao, L. Tsang, E. G. Njoku, A. Colliander, T. Jackson, M. S. Brugin, and S. Yueh, "Modelling and validation of combined active and passive microwave remote sensing of agricultural vegetation at L-band," *Progress In Electromagnetics Research B*, Vol. 78, 91–124, 2017.

27. Chen, K., L. Tsang, K. Chen, T. H. Liao, and J. Lee, "Polarimetric simulations of SAR at L-band over bare soil using scattering matrices of random rough surfaces from numerical three-dimensional solutions of Maxwell equations," *IEEE Transactions on Geoscience and Remote Sensing*, Vol. 52, No. 11, 7048–7058, Nov. 2014.

28. Liao, T.-H., L. Tsang, S. Huang, N. Niamsuwan, S. Jaruwatanadilok, S.-B. Kim, H. Ren, and K.-L. Chen, "Copolarized and cross polarized backscattering from random rough soil surfaces from L-band to Ku-band using numerical solutions of Maxwell's equations with near-field precondition," *IEEE Trans. Geosci. Rem. Sens.*, Vol. 54, No. 2, 651–662, Feb. 2016.

29. Kim, S.-B., J. J. Van Zyl, J. T. Johnson, M. Moghaddam, L. Tsang, A. Colliander, et al., "Surface soil moisture retrieval using the L-band synthetic aperture radar onboard the soil moisture active-passive satellite and evaluation at core validation sites," *IEEE Transactions on Geoscience and Remote Sensing*, Vol. 55, 1897–1914, 2017.

30. Duren, R., Ed. Wong, B. Breckenridge, S. Shaffer, C. Duncan, E. Tubbs, and P. Salomon, "Metrology, attitude, and orbit determination for spaceborne interferometric synthetic aperture radar," *SPIE AeroSense Conference on Acquisition, Tracking and Pointing*, Apr. 1998.